

1           **Spontaneous wave generation at strongly strained density fronts**

2                           Callum J. Shakespeare and John R. Taylor\*

3    *Department of Applied Mathematics and Theoretical Physics, University of Cambridge, Centre*  
4                           *for Mathematical Sciences,*  
5                           *Wilberforce Road, Cambridge CB3 0WA, UK*

6    \**Corresponding author address:* John R. Taylor, Department of Applied Mathematics and Theo-  
7    retical Physics, University of Cambridge, Centre for Mathematical Sciences, Wilberforce Road,  
8    Cambridge CB3 0WA, UK  
9    E-mail: J.R.Taylor@damtp.cam.ac.uk

## ABSTRACT

10 A simple analytical model is presented describing the spontaneous genera-  
11 tion of inertia-gravity waves at density fronts subjected to strong horizontal  
12 strain rates. The model considers fronts of arbitrary horizontal and vertical  
13 structure in a semi-infinite domain, with a single boundary at the ocean sur-  
14 face. Waves are generated due to the acceleration of the steady uniform strain  
15 flow around the density front, analogous to the generation of lee waves via  
16 flow over a topographic ridge. Significant wave generation only occurs for  
17 sufficiently strong strain rates,  $\alpha > 0.2f$ , and sharp fronts,  $H/L > 0.5f/N$ .  
18 The frequencies of the generated waves are entirely determined by the strain  
19 rate. The lowest frequency wave predicted to be generated via this mechanism  
20 has a Lagrangian frequency  $\omega = 1.93f$  as measured in a reference frame mov-  
21 ing with the background strain flow. The model is intended as a first-order de-  
22 scription of wave generation at submesoscale (1 to 10km wide) fronts where  
23 large strain rates are commonplace. The analytical model compares well with  
24 fully non-linear numerical simulations of the submesoscale regime.

## 25 **1. Introduction**

26 Recent observations and numerical simulations show significant inertia-gravity wave generation  
27 at density fronts (e.g. Alford et al. 2013; Danioux et al. 2012). Density fronts are regions of large  
28 horizontal density gradient, and are commonplace near the ocean surface. Wave generation at  
29 fronts is a potential mechanism for the transfer of energy from large-scale balanced flow to waves  
30 (e.g. Polzin 2010; Thomas 2012), some of which radiates from the surface into the deep ocean  
31 (Nagai et al. 2015). Once in the ocean interior, these waves contribute to the internal wave field  
32 which includes large contributions from wind and tides. Some of the internal wave energy might  
33 also be reabsorbed into the large-scale flow via wave-mean interactions (Booker and Bretherton  
34 1967; Nagai et al. 2015). The remaining internal waves from all sources are ultimately dissipated  
35 via breaking in the ocean interior, driving turbulence and mixing, and thus contributing to the  
36 maintenance of the global overturning circulation (Polzin and Lvov 2011; Wunsch and Ferrari  
37 2004).

38 The generation of waves at density fronts occurs through a variety of mechanisms including  
39 baroclinic instability of the front (e.g. Zhang 2004; Viudez and Dritschel 2006), non-linear pro-  
40 cesses at very sharp fronts (e.g. Snyder et al. 1993; Ford 1994), and forcing (e.g. from surface  
41 wind stresses or buoyancy fluxes) that varies rapidly in time (e.g. Snyder et al. 1993; Griffiths and  
42 Reeder 1996; Rossby 1938; Gill 1984; Blumen 2000) — for a detailed discussion of these and  
43 other wave generation processes the reader is referred to the review articles of Plougonven and  
44 Zhang (2014) and Vanneste (2013). Here we investigate the specific case of wave generation at  
45 fronts subject to strong confluent strain flows, defined by strain rates  $\alpha \sim f$ . In the present work,  
46 we will use the term ‘strain rate’ to describe the cross-frontal confluence — that is,  $\alpha \equiv -\partial_x u$  for  
47 a front oriented along the  $y$ -axis — and not the (larger) modulus of the strain rate tensor, which we

48 will call the ‘net strain rate’. The straining is considered to arise from a larger scale background  
49 flow — for example, an eddy field — which then acts on the relatively smaller scale front. A  
50 front in such a confluent strain field will sharpen with time in a process known as *frontogene-*  
51 *sis* (Hoskins and Bretherton 1972). Recent observations (e.g. Shcherbina et al. 2013; Hosegood  
52 et al. 2013; Rudnick and Luyten 1996; D’Asaro et al. 2011) and numerical simulations (e.g. Rosso  
53 et al. 2015; Capet et al. 2008; Gula et al. 2014; Mahadevan and Tandon 2006) have shown that  
54 large strain rates are commonplace on the ocean submesoscale, which is characterized by horizon-  
55 tal scales of 1 to 10km (see also the review article of Thomas et al. 2008). For example, Rosso  
56 et al. (2015) observe large-scale (mesoscale) net strain rates of up to  $0.4f$  in their submesoscale  
57 resolving numerical model, and show that the vertical velocity on the submesoscale is strongly  
58 correlated with the mesoscale strain rate, suggesting active submesoscale frontogenesis is present.  
59 Shcherbina et al. (2013) observe very large net strains — in places exceeding  $2f$  — although  
60 this figure is the net strain rate, including the self-strain associated with the submesoscale fronts  
61 (and other phenomena). Nonetheless, collectively these studies emphasize that both sharp density  
62 fronts and large strain rates are ubiquitous at small scales in the ocean surface layer. Here we  
63 develop a simple model that predicts significant wave generation at such strained fronts.

64 The classical quasi- and semi-geostrophic balance frontogenesis models (Williams and Plotkin  
65 1968; Hoskins and Bretherton 1972) assume that the strain rate is small, typically  $\alpha \sim 0.1f$ . In  
66 this limit, the frontal system remains close to geostrophic balance and no wave generation occurs.  
67 Wave generation at more strongly strained fronts has recently been investigated analytically by  
68 Shakespeare and Taylor (2013, 2014) and Shakespeare (2015a), motivated in-part by earlier nu-  
69 merical results (e.g. Snyder et al. 1993). These studies investigated the idealized problem of a  
70 uniform potential vorticity fluid with rigid lids at the top and bottom of the domain, and fronts  
71 on both boundaries. Shakespeare and Taylor (2013) examined the generation of waves in this

72 configuration due to the adjustment of unbalanced initial conditions for weakly strained fronts.  
73 Shakespeare and Taylor (2014) examined the same configuration, but for larger strain rates, and  
74 showed that waves are spontaneously generated as the surface front sharpens. The waves did not  
75 propagate vertically, owing to the presence of the rigid lids, and were also trapped horizontally  
76 by the confluent strain flow. The amplitude of the generated waves was found to be exponentially  
77 small for small strain rate, but substantial for larger strain rates. Shakespeare and Taylor (2015)  
78 confirmed these results by direct comparison with numerical simulations.

79 Here we introduce a model with two important differences to these previous models of strained  
80 internal fronts (Hoskins and Bretherton 1972; Shakespeare and Taylor 2013, 2014; Shakespeare  
81 2015a). Firstly, we consider a semi-infinite domain with a single boundary at the ocean sur-  
82 face. This is more readily applicable to the ocean than previous rigid lid models, and permits the  
83 downward propagation of waves generated at the surface front. Secondly, we allow non-uniform  
84 potential vorticity, which permits surface intensified fronts where the horizontal density gradient  
85 is maximum near the surface and decays with depth, as is typically the case for ocean fronts. To  
86 make the model analytically tractable, we linearize the equations of motion. The linearized equa-  
87 tions are only strictly valid in the limit of small geostrophic Rossby number,  $Ro_g = \Delta b H / (f^2 L^2)$ ,  
88 where  $\Delta b$  is the buoyancy difference across the front,  $H$  the frontal height and  $L$  the width. This  
89 assumption is unlikely to be valid for submesoscale fronts, where  $Ro_g$  is often order one (e.g.  
90 Shcherbina et al. 2013). However, comparison of the analytical model with a fully non-linear  
91 simulation of a submesoscale front (see §3) demonstrates that the analytic model is valid at depth,  
92 away from the surface front, and accurately describes the wave field. In other words, the dynamics  
93 of waves in the far field are largely unaffected by the locally large Rossby numbers and associ-  
94 ated non-linear dynamics at the front itself (a result also noted by Shakespeare and Taylor 2015;  
95 Shakespeare 2015a).

96 One objective of this paper is to investigate the dynamical mechanism responsible for the gener-  
97 ation of waves at strained fronts. In §2b we demonstrate the mathematical similarity of the present  
98 frontal wave problem to the classical rotating lee wave problem of Queney (1947). In the Queney  
99 (1947) model waves are generated when a uniform background flow passes over a topographic  
100 ridge. The background flow is accelerated around the ridge, into the stratified ambient, and for  
101 sufficiently sharp ridges (small width  $L$ ) and strong flow (large  $\bar{U}$ ) characterized by large Rossby  
102 number  $Ro = \bar{U}/(fL)$ , buoyancy forces give rise to a wave response (Queney 1947; Pierrehumbert  
103 1984; Muraki 2011). Here we show that a density front presents an obstacle to a background strain  
104 flow, in the same way a topographic ridge presents an obstacle to a uniform background flow. The  
105 background strain flow is accelerated around the density front into the stratified ambient, and for  
106 sufficiently sharp fronts and strong strain flows, buoyancy forces drive a wave response. Just like  
107 steady lee waves, these ‘frontal waves’ are trapped by the background flow in a distinctive pattern.  
108 The effect of a background strain flow on inertia-gravity waves has previously been considered by  
109 Plougonven and Snyder (2005) and Thomas (2012), among others. Here, we show that the strain  
110 field is responsible for both the generation and the trapping of the waves.

111 The paper is set out as follows. In §2 we derive the general linearized equation for the buoyancy  
112 field in a strained, quasi-two-dimensional flow. In §2a1 we write down the analytic solution for the  
113 special case of constant strain rate and stratification. The frequencies and amplitudes of generated  
114 waves can be determined directly from this solution, independent of the details of the frontal  
115 structure. We then explore the dependence of the wave generation on the strain rate (§2a2) and  
116 width of the surface front (§2a3). The dynamics of wave generation at internal fronts is compared  
117 to that at topographic obstacles in §2b. In §3 we compare the analytical model predictions with  
118 fully non-linear simulations of a submesoscale front. Lastly, in §4 we discuss the implications of  
119 these results for the generation of inertia-gravity waves in the ocean.

120 **2. Theory**

121 We begin our analysis with the incompressible, hydrostatic, Boussinesq equations for a rotating  
 122 fluid in Cartesian coordinates. Here, we will use  $(U, V, W)$  to denote the velocity components in  
 123 the  $(x, y, z)$  directions, respectively,  $B$  the buoyancy,  $P$  the pressure, and  $f$  the (constant) Coriolis  
 124 frequency. The variables are decomposed into background (denoted by an overbar) and pertur-  
 125 bation (denoted by lower case) components. The background state is one of uniform horizontal  
 126 strain rate,  $\bar{U} = -\alpha x$  and  $\bar{V} = \alpha y$  where  $\alpha$  may be a function of time, and background strati-  
 127 fication,  $N^2(z)$ , such that  $\bar{B} = \int N^2(z) dz$ . The perturbation to this background state, or frontal  
 128 anomaly — which includes the front, cross-frontal circulation and any internal wave field — is  
 129 assumed to be infinitely long and oriented along the  $y$ -axis such that the perturbation flow has no  
 130  $y$  dependence. With these assumptions the flow may be written as

$$U = \bar{U} + u(x, z, t), \quad V = \bar{V} + v(x, z, t), \quad W = w(x, z, t) \quad (1a)$$

$$P = \bar{P} + p(x, z, t), \quad b = \bar{B} + b(x, z, t), \quad (1b)$$

131 where the background pressure must be chosen as

$$\bar{P} = -\rho_0 \left( \frac{\alpha^2}{2} (x^2 + y^2) + \frac{\partial_t \alpha}{2} (y^2 - x^2) - \alpha f x y - \int \bar{B} dz \right), \quad (2)$$

132 such that the background state independently (i.e. when the perturbation variables are identically  
 133 zero) satisfies the inviscid Boussinesq equations. Substituting the net fields (1) into the Boussinesq  
 134 equations and simplifying yields the governing equations for the two-dimensional perturbation

135 fields,

$$Du = fv + \alpha u - \frac{1}{\rho_0} \frac{\partial p}{\partial x} + v_h \frac{\partial^2 u}{\partial x^2}, \quad (3a)$$

$$Dv = -fu - \alpha v + v_h \frac{\partial^2 v}{\partial x^2}, \quad (3b)$$

$$0 = -\frac{1}{\rho_0} \frac{\partial p}{\partial z} + b, \quad (3c)$$

$$Db = -N^2(z)w + \kappa_h \frac{\partial^2 v}{\partial x^2}, \quad (3d)$$

$$0 = \frac{\partial u}{\partial x} + \frac{\partial w}{\partial z}, \quad (3e)$$

136 where  $D \equiv \partial_t + (u + \bar{U}) \partial_x + w \partial_z$  is the material derivative. The  $\kappa_h$  and  $v_h$  are the artificial hori-  
 137 zontal diffusivity and viscosity that will be used for the numerical solutions in §3. The equations  
 138 (3) are identical to those examined by previous authors (for example, the numerical study of Snyder  
 139 et al. 1993, their equation 2; the only difference being that here we have the additional assump-  
 140 tions of incompressibility and hydrostatic balance). The five equations for the perturbation fields  
 141 (3) involve five independent variables:  $u, v, w, p, b$ .

142 For the analytic model, we consider the inviscid case ( $\kappa_h = v_h = 0$ ) and make a number of  
 143 simplifying assumptions. The objective is to formulate the simplest possible model for wave  
 144 generation at fronts. With that aim, here we consider the situation where the perturbation flow,  
 145  $u$ , is small compared with the background strain flow,  $u \ll \bar{U}$ , such that equations (3) become  
 146 linear (following Shakespeare 2015a), with the material derivative only involving advection by the  
 147 background flow,  $D \equiv \bar{D} = \partial_t + \bar{U} \partial_x$ . For an inviscid, weakly strained front, this assumption is  
 148 equivalent to the usual quasi-geostrophic (QG) approximation that the Rossby number is small.  
 149 Assuming that time scales with the inverse strain rate or *advective timescale*,  $1/\partial_x \bar{U} = 1/\alpha$ , and  
 150 that the strain rate is small relative to the Coriolis frequency,  $\alpha \ll f$ , (3a) implies that the along-  
 151 front velocity  $v$  scales geostrophically,  $v \sim \Delta b H / (fL)$ , while (3b) implies that  $u \sim \alpha / f v$ . For

152 the linear model to be strictly valid we require  $u \ll \bar{U}$ , or substituting the derived scales,  $Ro_g =$   
 153  $\Delta bH/(f^2 L^2) \ll 1$ . However, unlike previous linear QG models (e.g. Williams and Plotkin 1968),  
 154 we make no assumption about the strain rate  $\alpha$  in comparison to the inertial frequency  $f$ .

155 It is easily shown from the linearized equations (3) that the perturbation potential vorticity (PV)  
 156 is conserved, or

$$\bar{D}q = 0, \text{ where } q = fN^2(z) \frac{\partial}{\partial z} \left( \frac{b}{N^2(z)} \right) + N^2(z) \frac{\partial v}{\partial x}. \quad (4)$$

157 Equation (4) implies that the PV evolves according to  $\partial_t q - \alpha x \partial_x q = 0$ , or that  $q = q_0(x e^{\beta(t)}, z)$ ,  
 158 where  $q_0(x, z)$  is the initial PV distribution and  $\beta$  is the non-dimensional strain,  $\beta(t) = \int_0^t \alpha(t') dt'$ .  
 159 Thus, the action of the strain flow is to squeeze a PV anomaly with time. Usually such a PV  
 160 anomaly will be associated with a density front. For consistency with previous work (Shakespeare  
 161 and Taylor 2013, 2014, 2015; Shakespeare 2015a), here we define the frontal buoyancy anomaly  
 162 associated with the PV as

$$b_0(x, z) = \frac{N^2(z)}{f} \int_{-\infty}^z \frac{q_0(x, z')}{N^2(z')} dz', \quad (5)$$

163 such that the net perturbation buoyancy field,  $b$ , is

$$b(x, z, t) = b_0(x e^{\beta}, z) + b'(x, z, t), \quad (6)$$

164 where  $b'$  is the buoyancy response to the imposed PV anomaly. The above definition of  $b_0$  (5) is an  
 165 entirely arbitrary — but mathematically convenient — subdivision of the perturbation buoyancy  
 166  $b$  in an ‘imposed anomaly’  $b_0$  and ‘response’  $b'$  and implies no additional assumptions about the  
 167 flow. The objective now is to formulate an equation for the evolution of  $b'$  forced by the strain-  
 168 driven sharpening of the frontal anomaly  $b_0$ .

169 The buoyancy response  $b'$  may be related to the along-front velocity,  $v$ , by substitution of (6)  
 170 into the PV equation (4):

$$\frac{\partial v}{\partial x} = -f \frac{\partial}{\partial z} \left( \frac{b'}{N^2(z)} \right). \quad (7)$$

171 The solution proceeds by taking the material derivative of the  $y$ -momentum equation (3b), and  
 172 substituting the  $x$ -momentum equation (3a), to obtain

$$(\bar{D}^2 + f^2 - \alpha^2 + \partial_t \alpha) v = \frac{f}{\rho_0} \frac{\partial p}{\partial x}. \quad (8)$$

173 We now take an  $x$  and  $z$  derivative of (8), and substitute  $\partial_x v$  from (7) and  $\partial_z p$  from (3c), yielding  
 174 an equation for  $b'$ :

$$(\bar{D}^2 - 2\alpha\bar{D} + f^2) \frac{\partial^2}{\partial z^2} \left( \frac{b'}{N^2(z)} \right) + \frac{\partial^2 b'}{\partial x^2} = -\frac{\partial^2}{\partial x^2} b_0(xe^\beta, z). \quad (9)$$

175 Equation (9) may be solved numerically for a given choice of initial conditions, buoyancy anomaly  
 176  $b_0$ , strain rate  $\alpha(t)$ , and stratification  $N^2(z)$ . In the next section we derive an analytic solution for  
 177 the special case of constant strain rate and stratification.

#### 178 *a. Constant strain rate and stratification*

179 Here we will first consider an infinite domain in both  $x$  and  $z$ . As will be described below, the  
 180 semi-infinite domain solution with a rigid lid at  $z = 0$  may be obtained directly from the infinite  
 181 domain solution. Taking the Fourier transform of (9) in  $x$  and  $z$  (with  $N^2$  and  $\alpha$  constant) yields

$$\left[ \left( \widehat{D}^2 - 2\alpha\widehat{D} + f^2 \right) \frac{-m^2}{N^2} - k^2 \right] \widehat{b}' = k^2 e^{-\alpha t} \widehat{b}_0(k e^{-\alpha t}, m), \quad (10)$$

182 where  $k$  and  $m$  are the horizontal and vertical wavenumbers, respectively, hats denote the Fourier  
 183 transform, and  $\widehat{D} = \partial_t + \alpha(1 + k\partial_k)$  is the transformed material derivative. The general solution  
 184 (Shakespeare 2015b, §6.2.1) to the PDE (10) for  $\{\alpha, m, N\} \neq 0$  is

$$\begin{aligned} \widehat{b}'(k, m, t) = & \underbrace{-\varepsilon^2 \left( G(\varepsilon) \left[ e^{-\alpha t} \widehat{b}_0(k e^{-\alpha t}, m) \right] \right)}_{\text{forced}} \\ & + \underbrace{H_+(\varepsilon) \left[ e^{-\alpha t} c_1(k e^{-\alpha t}, m) \right] + H_-(\varepsilon) \left[ e^{-\alpha t} c_2(k e^{-\alpha t}, m) \right]}_{\text{adjustment waves}}, \end{aligned} \quad (11)$$

185 where  $\varepsilon = Nk/(fm)$ , and the  $c_i$  are unknown functions dependent on the choice of initial con-  
186 ditions.<sup>1</sup> The solution (11) contains two parts. The ‘forced’ part is defined by the requirement  
187 that time dependence only arises through the strain-driven sharpening of the buoyancy (and PV)  
188 anomaly,  $b_0(xe^{\alpha t}, z)$ , as per the forcing to the right-hand side of (9) and (10). The remaining ‘ad-  
189 justment wave’ part of (11) describes propagating waves generated due to the adjustment of initial  
190 conditions that differ from those implied by the forced solution, analogous to the waves generated  
191 during geostrophic adjustment. The unusual form of the wave solutions in (11) is due to the fact  
192 that the strain field modifies the propagation of, and ultimately traps the waves — these dynamics  
193 were studied in a similar context in Shakespeare and Taylor (2013, see section 4.2 and figure 15  
194 therein). In the present work, our focus is on waves generated in response to strain forcing rather  
195 than via adjustment of initial conditions, and thus here we will only consider the forced part of the  
196 flow.

197 The functions  $G$  and  $H_{\pm}$  in (11) are obtained by substitution of (11) into the PDE (10), yielding  
198 the ODE:

$$\left[ \varepsilon^2 \delta^2 \frac{\partial^2}{\partial \varepsilon^2} + 3\delta^2 \varepsilon \frac{\partial}{\partial \varepsilon} + 1 + \varepsilon^2 \right] G(\varepsilon) = -1, \quad (12)$$

199 where  $\delta = \alpha/f$  is the non-dimensional strain rate (also called the ‘strain Rossby number’). The  
200 particular and homogeneous solutions to (12) are, respectively,

$$G(\varepsilon) = -1 + \frac{\varepsilon^2}{1 + 8\delta^2} {}_1F_2 \left( 1; \left( \frac{5}{2} - \frac{\iota\sigma}{2}, \frac{5}{2} + \frac{\iota\sigma}{2} \right); -\frac{\varepsilon^2}{4\delta^2} \right), \quad (13)$$

$$H_{\pm}(\varepsilon) = \frac{1}{\varepsilon} J_{\pm\sigma\iota} \left( \frac{\varepsilon}{\delta} \right), \quad (14)$$

201 where  ${}_pF_q$  is the generalized hypergeometric function,  $J$  is the Bessel function of complex order,  
202 and  $\sigma = \sqrt{(f/\alpha)^2 - 1}$ . The choice of the particular solution to (12),  $G(\varepsilon)$ , is unique in that it is

---

<sup>1</sup>This solution structure emerges due to the form of the material derivative in the linearized system; i.e.  $\widehat{D} \left[ e^{-\alpha t} \widehat{F}(ke^{-\alpha t}, m) \right] = 0$  for any  $\widehat{F}$ ,  
which is the Fourier equivalent of  $\widehat{D}[F(xe^{\alpha t}, z)] = 0$ .

203 the only solution to (12) that is finite at  $\varepsilon = 0$ , implying that the forced solution is also unique as  
 204 explained below.

## 205 1) GREEN'S FUNCTIONS

206 The forced part of the solution (11) can be rewritten in terms of the along-front shear, by Fourier  
 207 transforming (7) to yield

$$\widehat{\partial_z v} = ik\widehat{b'}/(f\varepsilon^2) = f^{-1}G(\varepsilon) \left[ -ike^{-\alpha t}\widehat{b}_0(ke^{-\alpha t}, m) \right]. \quad (15)$$

208 The function  $\widehat{\partial_z v}_G = f^{-1}G(\varepsilon)$  in (15), with  $G$  defined by (13), is the *Green's function* for the  
 209 along-front shear. It contains all the dynamics and structure of the forced response, independent  
 210 of the details of the buoyancy anomaly  $b_0$ . The Green's function depends only on the scaled  
 211 wavenumber,  $\varepsilon = kN/(fm)$ , which can be thought of as the Burger number, or scaled slope, of a  
 212 given mode  $(k, m)$ . In physical space, the solution (15) may be written as a double convolution of  
 213 the Green's function with the buoyancy gradient anomaly,

$$\partial_z v(x, z, t) = \int_{-\infty}^{\infty} \int_{-\infty}^{\infty} \partial_z v_G(x - x_0, z - z_0) \frac{\partial}{\partial x_0} b_0(x_0 e^{\alpha t}, z_0) dx_0 dz_0. \quad (16)$$

214 A valid solution for the along-front shear requires that its integral over all  $x$  has a finite value.  
 215 The integral over all  $x$  is equal to the  $k = \varepsilon = 0$  value of its spectrum,  $\widehat{\partial_z v}(0)$  in (15). The square  
 216 bracketed factor in (15) corresponds to the buoyancy anomaly gradient. Again, the  $k = \varepsilon = 0$  value  
 217 of this factor is the integral over all  $x$  of the buoyancy gradient:  $\int_{-\infty}^{\infty} \partial_x b_0(xe^{\alpha t}, z) dx = \Delta b(z)$ , the  
 218 buoyancy difference across the front, which is finite and invariant time. For  $\widehat{\partial_z v}(0)$  to be finite we  
 219 thus require that  $G(0)$  is finite. The only possible solution for  $G(\varepsilon)$  is therefore that defined by  
 220 (13), since the  $H_{\pm}(\varepsilon)$  homogeneous solutions (14) are infinite at  $\varepsilon = 0$ . The forced solution (15)  
 221 is therefore unique and its properties controlled by the Green's function  $G(\varepsilon)$  (13).

222 Green's functions for other fields may also be written as derivatives of  $G(\varepsilon)$ . For instance, since  
 223  $u = -f^{-1}(\bar{D} + \alpha)v$  from (3b), it may be shown that the Green's function for the cross-front shear  
 224 is defined by

$$\widehat{\partial_z u}_G = -f^{-1} \delta \left( \varepsilon \frac{\partial}{\partial \varepsilon} + 2 \right) G(\varepsilon). \quad (17)$$

225 Similarly, the Green's function for the divergence may be derived from continuity (3e) and satis-  
 226 fies,

$$\widehat{\partial_x u}_G = -\widehat{\partial_z w}_G = -N^{-1} \delta \varepsilon \left( \varepsilon \frac{\partial}{\partial \varepsilon} + 2 \right) G(\varepsilon). \quad (18)$$

227 Note that the motivation for using the shears and divergences of the velocity fields in the above  
 228 expressions, rather than the velocities themselves, is that the former depend only on the scaled  
 229 mode slope,  $\varepsilon = Nk/(fm)$ , whereas the latter depend on the individual horizontal and vertical  
 230 wavenumbers.

231 The non-dimensional Green's function for the cross-front shear,  $f \widehat{\partial_z u}_G$ , is shown in figure 1. The  
 232 behavior of the Green's function depends strongly on the magnitude of the strain rate. For small  
 233 strain rates,  $\delta \sim 0.1$ , the function decays smoothly to zero with increasing scaled mode slope  $\varepsilon$ . For  
 234 larger strain rate,  $\delta \geq 0.2$ , the Green's function is smoothly decreasing for small slopes  $\varepsilon < 1$  but  
 235 exhibits high-amplitude oscillations in the region  $\varepsilon > 1$ , implying the accumulation of energy at  
 236 certain preferential wavenumber combinations,  $\varepsilon = Nk/(fm)$ , or resonant modes. As will be seen  
 237 below, these oscillations correspond to a set of stationary waves with phase slopes of  $k/m = f\varepsilon/N$   
 238 and Lagrangian frequencies  $\omega = f\sqrt{1 + \varepsilon^2}$ <sup>2</sup>. The logarithmic color scale in figure 1 indicates that  
 239 the amplitude of the oscillations (and therefore waves) is *exponentially small* at small strain rate  
 240 (consistent with the result derived in the rigid-lid case studied in Shakespeare and Taylor 2014).

---

<sup>2</sup>Here, the Lagrangian frequency denotes the frequency a wave would have if it were observed in a reference frame moving with the background flow, as opposed to the Eulerian frequency which is the frequency that is observed at a fixed point in space. This distinction will become important in subsection 4 below.

241 The differing behavior at small and large strain rate is captured by the two asymptotic limits. In  
 242 the limit of vanishingly small strain rate,  $\delta \rightarrow 0$ , the Green's function asymptotes to a smoothly  
 243 decaying profile,

$$G(\varepsilon) = -\frac{1}{1 + \varepsilon^2}, \quad (19)$$

244 and corresponds to an along-front velocity in geostrophic balance with the buoyancy anomaly (i.e.  
 245 the Williams and Plotkin (1968) solution). In contrast, the Green's function for large strain rate,  
 246  $\delta \rightarrow \infty$ , asymptotes to an oscillation-dominated profile,

$$G(\varepsilon) = -\frac{2\delta}{\varepsilon} J_1\left(\frac{\varepsilon}{\delta}\right), \quad (20)$$

247 where  $J_1$  is the 1st order Bessel function.

## 248 2) STRAIN RATE DEPENDENCE

249 To construct the full solution from the Green's functions, we require knowledge of the structure  
 250 of the buoyancy gradient anomaly,  $\partial_x b_0$ , at some instant in time. The solution at that time is  
 251 given by the convolution of the anomaly with the Green's function, as per (15) and (16). We are  
 252 primarily interested in solutions in the semi-infinite domain  $z \leq 0$ , with a rigid-lid representing the  
 253 ocean surface at  $z = 0$ . Here we will consider a simple surface-intensified buoyancy anomaly, or  
 254 front, of the form

$$b_0(x, z) = \frac{\Delta b_0}{2} \exp\left(-\left(\frac{z}{H}\right)^2\right) \operatorname{erf}\left(\varepsilon_F \frac{x}{L_R}\right), \quad (21)$$

255 where  $H$  is the height scale of the front,  $\Delta b_0$  is the change in buoyancy across the front and  
 256  $L_R = NH/f$  is the Rossby radius. The parameter  $\varepsilon_F = L_R/L$  is the Burger number, or characteristic  
 257 slope, of the frontal anomaly. Solutions for the semi-infinite domain can be generated using the  
 258 solutions in the previous section by mirroring the buoyancy anomaly defined for  $z \leq 0$  into the  
 259 region  $z > 0$ ; that is, multiplying  $b_0$  by  $-\operatorname{sign}(z)$ .<sup>3</sup> This process ensures that the solution contains

---

<sup>3</sup>This is equivalent to changing the vertical Fourier transform to a sine transform.

260 only odd (sine) vertical modes, and thus enforces the rigid-lid boundary condition of  $w = 0$  at  
261  $z = 0$ .

262 The vertical velocity fields for a frontal Burger number ( $\epsilon_F$ ) of 1 and strain rates of (a)  $0.1f$ ,  
263 (b)  $0.3f$  and (c)  $1.0f$  are shown in figure 2. For the small strain rate case ( $\alpha = 0.1f$ , figure 2a)  
264 the velocity is dominated by an ascending jet of large vertical velocity on the warmer (right-hand)  
265 side of the front, and a descending jet on the cooler side, consistent with the classical paradigm  
266 of the thermally-direct secondary circulation about a strained front. The larger strain rates show a  
267 similar circulation about the surface front, but the steepness and strength of the jets is increased.  
268 In addition the larger strain rate solutions exhibit banded structures at depth, which correspond to  
269 horizontally trapped inertia-gravity waves. The amplitude of these waves is substantially less than  
270 the secondary circulation for moderate strain rate ( $\alpha = 0.3f$ , figure 2b), but of similar order for  
271 large strain rate ( $\alpha = 1.0f$ , figure 2c). Note that the amplitude of the secondary circulation (vertical  
272 velocity magnitude) in each case can be significantly larger if non-linear effects are considered,  
273 owing to the non-linear sharpening of the surface front (see §3).

274 The strain rate influences the strength and steepness of the near-surface jets of vertical velocity  
275 and hence the regions of largest divergence,  $\partial_z w$ . The influence of the strain on the divergence  
276 can be predicted directly from the divergence Green's function (18). For small strain rates, the  
277 divergence Green's function has a single extremum in  $\epsilon$  — since there are no waves in the flow,  
278 this extremum must correspond to the jets of large vertical velocity associated with the secondary  
279 circulation. As the strain rate is increased, this extremum is retained, but additional extrema begin  
280 to appear at larger  $\epsilon$ . We interpret these additional extrema as corresponding to the resonant  
281 wave modes of the system, as will be examined in more detail below.<sup>4</sup> Nonetheless, for now

---

<sup>4</sup>However, note that uniquely defining the 'wave' flow in the present system is problematic, as has been discussed previously by Shakespeare and Taylor (2014).

282 we extract the  $\varepsilon$  for which the first extremum (in  $\varepsilon$ ) in the divergence Green's function occurs at  
 283 each value of strain rate. The slope of the vertical velocity jets,  $k/m = f\varepsilon/N$ , predicted by this  
 284 method is indicated by grey lines in figure 2. More generally, the jet slope as a function of strain  
 285 rate is shown in figure 3a. The slope is constant for small strain rate, but increases linearly at  
 286 large strain rate. The asymptotic limits (indicated by dashed lines on the figure) may be derived  
 287 directly from the asymptotic Green's functions. In the limit  $\delta \rightarrow 0$  (19) the local maxima of  
 288 the divergence Green's function is located at  $\varepsilon = 1/\sqrt{3}$ , implying that the jets have a slope of  
 289  $k/m = f/(N\sqrt{3}) \simeq 0.58 f/N$ . In this limit, the scale of the frontal circulation is largely unaffected  
 290 by the presence of the (weak) strain flow. For large strain rate,  $\delta \rightarrow \infty$ , (20) the jets are steeper,  
 291 with slope  $k/m \simeq 1.26 \alpha/N$ . In this limit, the convergent strain flow strongly confines the frontal  
 292 circulation in the horizontal, leading to steeper, intensified jets.

293 The vertical velocity magnitude (jet strength) may also be estimated from the Green's function  
 294 as the local maximum value of the divergence, and is plotted in figure 3b. The vertical velocity  
 295 increases linearly at small strain rate and quadratically at large strain rate. The linear increase at  
 296 small strain rate is predicted from quasi- and semigeostrophic models of frontogenesis (Williams  
 297 and Plotkin 1968; Hoskins and Bretherton 1972) and is merely a requirement of continuity: a  
 298 larger background strain flow implies a correspondingly larger secondary circulation to conserve  
 299 volume at the front, since a greater volume of fluid must be deflected down and around the frontal  
 300 anomaly. The additional (quadratic) increase in vertical velocity at large strain rate is associated  
 301 with the linear increase in the slope of the jets, which is due to the strong strain flow confining the  
 302 secondary circulation around the strain axis, as noted above. While non-linear effects will modify  
 303 the magnitude of the secondary circulation (see §3), the confinement effect of the strain flow will  
 304 still operate (as shown in the numerical simulations of Shakespeare and Taylor 2015), and thus the  
 305 qualitative dependence of the secondary circulation on the strain rate described here is expected to

306 be robust. Indeed, figure 3b is qualitatively similar to the results of Rosso et al. (2015), in particular  
 307 their figure 5b, which displays the dependence of the vertical velocity on the large-scale strain rate  
 308 in their submesoscale-resolving numerical model of a sector of the Southern Ocean. The strain  
 309 rate dependence of the vertical velocity predicted here may thus have application in parameterizing  
 310 vertical velocities associated with fronts in ocean models of sufficiently high resolution to allow  
 311 fronts to form, but with insufficient resolution to accurately model the frontal circulation.

312 The slopes and Lagrangian frequencies of the waves (resonant modes) as a function of strain  
 313 rate can also be determined by computing the local extrema of the Green’s function for the cross-  
 314 frontal shear (17) shown in figure 1. This technique works since the waves visible in the solutions  
 315 (e.g. figure 2) are associated with a local maximum in the cross-frontal shear, as well as the  
 316 vertical velocity and divergence.<sup>5</sup> In figure 4 we plot the frequencies and amplitudes of the six  
 317 lowest frequency resonant modes of *significant* amplitude — we cannot rule out the presence  
 318 of lesser amplitude, lower frequency modes that are obscured by the secondary circulation and  
 319 which therefore do not generate extrema in the Green’s function spectrum. The Lagrangian wave  
 320 frequency is related to the scaled wave slope via  $\omega = f\sqrt{1 + \varepsilon^2}$ . The lowest Lagrangian frequency  
 321 associated with a distinct wave mode is  $1.93f$  and occurs for a strain rate of approximately  $0.3f$   
 322 (the strain rate used in figure 2b). For strain rates in the range  $0.2f < \alpha < f$ , the lowest frequency  
 323 distinct mode has a Lagrangian frequency less than  $4f$ . The wave slopes predicted from figure 4  
 324 are indicated as grey lines on the vertical velocity plots in figure 2b,c.

### 325 3) FRONTAL SCALE DEPENDENCE

326 In this section we address the question of how the frontal Burger number, or characteristic frontal  
 327 slope,  $\varepsilon_F = L_R/L = NH/(fL)$ , affects the solution for a given value of strain rate. The confluent

---

<sup>5</sup>Using the Green’s function for the divergence instead of the cross-frontal shear does not produce substantially different results.

328 strain acts to compress the horizontal scale  $L$  of the frontal buoyancy gradient anomaly  $\partial_x b_0$  with  
 329 time as per (16). The Burger number of the front will thus increase with time according to  $\varepsilon_F =$   
 330  $\varepsilon_{F,0} e^{\alpha t}$ . In other words, there is a one-to-one relationship between the frontal scale and time.  
 331 Thus, examining the Burger number dependence of the solution will also tell us about the time  
 332 evolution of the front.

333 Figure 5 displays the vertical velocity fields for a front subject to a strain rate of  $\alpha = 0.4f$ , for  
 334 five frontal scales (or time snapshots). The buoyancy anomaly is the same as used previously (21).  
 335 When the frontal width is large compared to the Rossby radius (a,  $L = 10L_R$ ; b,  $L = 5L_R$ ), the  
 336 secondary circulation is broad and relatively weak. In particular, for wide fronts ( $L \gg L_R$ ), there  
 337 are no waves present. As the frontal width approaches the Rossby radius (c,  $L = 2L_R$ ), the lowest  
 338 frequency (primary) wave mode appears. As the frontal width is reduced further (d,  $L = L_R$ ; e,  
 339  $L = 0.5L_R$ ), the primary wave mode amplifies and higher frequency packets appear. We observe  
 340 that the slopes (indicated on the figure by dashed grey lines) of both the frontal jets and the waves  
 341 are independent of the frontal width, implying that the vertical scale of the flow decreases at the  
 342 same rate as the horizontal to keep the slope constant.

343 This behavior may be understood by considering the form of the solution (15). The solution at  
 344 a given time is defined by the product of the Green's function and the buoyancy gradient anomaly  
 345 spectra evaluated at that instant in time. The possible slopes of the jets and waves are controlled  
 346 by the structure of the Green's function at a given value of the strain rate, whereas the amplitude of  
 347 those features is controlled by the spectral amplitude of the buoyancy gradient anomaly at the cor-  
 348 responding wavenumber combinations. For instance, the amplitude of a wave mode with a given  
 349 slope,  $\varepsilon = Nk/(fm)$ , is determined by the integrated amplitude in the buoyancy gradient spectrum,  
 350  $\widehat{\partial_x b_0}(k, m)$ , along the line  $m = Nk/(f\varepsilon)$ . As the frontal scale is reduced, the gradient spectrum has  
 351 more amplitude at higher horizontal wavenumbers  $k$ , and therefore more amplitude at steeper

352 slopes. Since, as shown in figure 1, wave modes are only present in the region  $\varepsilon = Nk/(fm) > 1$ ,  
 353 the spontaneous generation of waves can only occur for fronts with significant spectral amplitude  
 354 at the corresponding wavenumbers. Fronts that satisfy this requirement are characterized by order  
 355 one Burger numbers,  $\varepsilon_F \sim 1$ . Thus, as seen in figure 5, significant spontaneous wave genera-  
 356 tion via the present mechanism is only observed for fronts with widths comparable to the Rossby  
 357 radius, or smaller.

#### 358 4) RAY TRACING AND WAVE TRAPPING

359 Here we apply ray tracing theory to demonstrate that the resonant wave modes seen in the above  
 360 solutions correspond to wave packets that are generated at (or near) the front, and are confined  
 361 horizontally by the strain flow. Our analysis follows that of Reeder and Griffiths (1996) who  
 362 studied a very similar strained front system but via a numerical approach. The equations governing  
 363 the propagation of a wave packet in the  $xz$  plane are

$$\left(\frac{D}{Dt}\right)_g k = -\frac{\partial\Omega}{\partial x}, \quad (22a)$$

$$\left(\frac{D}{Dt}\right)_g m = -\frac{\partial\Omega}{\partial z}, \quad (22b)$$

$$\left(\frac{D}{Dt}\right)_g x = \frac{\partial\Omega}{\partial k}, \quad (22c)$$

$$\left(\frac{D}{Dt}\right)_g z = \frac{\partial\Omega}{\partial m}, \quad (22d)$$

364 where  $(D/Dt)_g$  is the material derivative following a packet, which propagates with speed  $\vec{c}_g =$   
 365  $(\partial_k\Omega, \partial_m\Omega)$  as per (22)c,d, and  $\Omega$  is the appropriately Doppler shifted (or Eulerian) frequency. For  
 366 the strain flow used here the Doppler shifted frequency is

$$\Omega = \omega(k, m) - \alpha kx, \quad \text{where } \omega(k, m) = \pm f \sqrt{1 + \left(\frac{Nk}{fm}\right)^2}, \quad (22e)$$

367 is the regular hydrostatic dispersion relation for inertia-gravity waves. We note that here, consis-  
368 tent with our basic model, we assume hydrostatic dynamics in our ray-tracing equations, and thus  
369 our ray-tracing analysis is only valid for sufficiently large horizontal scales (or small times). A  
370 discussion of non-hydrostatic effects is beyond the scope of this paper and the interested reader  
371 is referred to Shakespeare (2015a). Note that (22) are only valid for fronts of sufficiently small  
372 Rossby number such that the front does not directly affect the wave dispersion relation. Waves  
373 generated at stronger fronts may be trapped within the front (Kunze 1985; Whitt and Thomas  
374 2013) rather than propagating away. For a detailed derivation of the above equations (22), which  
375 are identical to equations 20, and 25 through 28, of Reeder and Griffiths (1996), the reader is  
376 referred to that paper. The ray tracing equations (22) may be solved explicitly to determine the  
377 behavior of a wave packet in the flow. Supposing the packet has initial wavenumbers  $(k_0, m_0)$ ,  
378 (22)a,b imply that the wave numbers at some later time are

$$k = k_0 e^{\alpha t}, \text{ and } m = m_0. \quad (23)$$

379 Thus, the action of the barotropic strain flow is to exponentially increase the horizontal wavenum-  
380 ber with time, without altering the vertical wavenumber (as described by Reeder and Griffiths  
381 1996; Plougonven and Snyder 2005; Thomas 2012, among others). We can now substitute the  
382 above results (23) into (22)c to obtain a differential equation for the  $x$ -position of the wave packet,

$$\left(\frac{D}{Dt}\right)_g x = \pm e^{-\alpha t} \frac{\partial \omega(k_0 e^{\alpha t}, m_0)}{\partial k_0} - \alpha x \implies \left(\frac{D}{Dt}\right)_g (x e^{\alpha t}) = \pm \frac{\partial \omega(k_0 e^{\alpha t}, m_0)}{\partial k_0}. \quad (24)$$

383 Equation (24) may be directly integrated in time<sup>6</sup> to obtain

$$x = x_0 e^{-\alpha t} \pm \frac{e^{-\alpha t}}{\alpha k_0} (\omega(k_0 e^{\alpha t}, m_0) - \omega(k_0, m_0)), \quad (25a)$$

384 where  $x_0$  is the initial horizontal location of the wave packet (this result was also obtained by  
385 Shakespeare 2015a, equation 15 therein). Following the same procedure for (22)d yields the  $z$ -

---

<sup>6</sup>Note that the initial wavenumbers  $k_0$  and  $m_0$  are constants with respect to the material derivative  $(D/Dt)_g$ .

386 position of the wave packet as a function of time

$$z = z_0 - \frac{1}{m_0 \alpha} (\omega(k_0 e^{\alpha t}, m_0) - \omega(k_0, m_0)), \quad (25b)$$

387 where  $z_0$  is the initial vertical location of the wave packet. We anticipate that wave packets will  
 388 be generated at the origin (where the front is located) such that  $x_0 = z_0 = 0$ , although the exact  
 389 time of generation is unclear. Using the nomenclature of previous sections the Burger number  
 390 of a given wave packet is  $\varepsilon_{wp} = Nk_0 e^{\alpha t} / (f m_0)$ . Regardless of exactly when the wave packet is  
 391 generated (25) implies that the packet will only propagate away from the origin when  $\varepsilon_{wp}$  is or-  
 392 der one or larger, since when  $\varepsilon_{wp} \ll 1$  the Lagrangian frequency  $\omega(k_0 e^{\alpha t}, m_0)$  is close to inertial  
 393 (and is equal to the initial frequency  $\omega(k_0, m_0)$ , and thus the location of the packet defined by (25)  
 394 is close to zero). This result is consistent with our observation in previous sections that waves  
 395 are only observed in the solution when the front is sufficiently sharp, defined by  $\varepsilon \sim 1$ . Further-  
 396 more, (25) shows how the packet is confined horizontally by the confluent strain flow; taking the  
 397 large time limit of (25a) yields  $x \rightarrow N / (\alpha m_0)$ . Thus a wave packet of vertical wavenumber  $m_0$   
 398 ultimately stagnates (horizontally) at a point in the flow where its maximum hydrostatic horizon-  
 399 tal group speed,  $N / m_0$ , equals the strain flow speed,  $\alpha x$  (this is only true for hydrostatic fluids;  
 400 see Shakespeare 2015a). The packet is not confined vertically, and indeed the vertical position  
 401 of the packet increases exponentially,  $z \rightarrow -Nk_0 e^{\alpha t} / (\alpha m_0^2)$  at large time (25b) as a result of the  
 402 barotropic straining field.

403 In figure 5 we plot the path of a single wave packet, which we assume to be generated at the  
 404 origin at time zero (figure 5a). We choose initial wavenumbers of  $k_0 = 0.2 / L_R$  and  $m_0 = 0.5 / H$   
 405 corresponding to an initial scale consistent with the scale of the secondary circulation in figure  
 406 5a. The path of the wave packet predicted by (25) is displayed as a solid black line on 5b to  
 407 e, with the terminus of the line denoting the position of the wave packet at the time each flow

408 snapshot is taken. The terminus of the ray path on each plot roughly approximates the position of  
409 the deepest, gravest phase lines that appear as time increases. In other words, the chosen vertical  
410 wavenumber  $m_0$  corresponds to the largest, and therefore fastest propagating, in the system. The  
411 ray path also approximately captures the horizontal spread of the wave energy at late time (figure  
412 5e). As predicted by the above theory the ray asymptotes to  $N/(\alpha m_0) = 5L_R$  at late time. Of  
413 course, the solution will contain waves with a range of vertical wavenumbers  $m_0$ , the spectrum of  
414 which will be set by the vertical structure of the front. Wave packets with higher  $m$  will propagate  
415 more slowly in the vertical, and be confined horizontally closer to the origin. Thus, as seen in  
416 figure 5c,d,e, these additional packets will modify the wave phase lines in that region after the  
417 fastest packet has already propagated past.

418 *b. Comparison with rotating lee waves*

419 It is useful to compare the present mechanism of spontaneous generation to other well known  
420 mechanisms, specifically ‘lee wave’ generation associated with flow across topography in a ro-  
421 tating system. The classical rotating lee wave model of Queney (1947) describes the steady state  
422 associated with a uniform background flow,  $\bar{U} = U_0$ , passing over a topographic ridge,  $z = h(x)$ ,  
423 on an  $f$ -plane. The equation for the perturbation buoyancy,  $b = B - N^2z$ , is

$$\left[ \underbrace{(\bar{D}^2 + f^2)}_{accel.} \underbrace{\frac{1}{N^2} \frac{\partial^2}{\partial z^2} + \frac{\partial^2}{\partial x^2}}_{geostrophic} \right] b = 0, \quad (26)$$

424 where  $\bar{D} = U_0 \partial_x$  at steady state. The equation is composed of two parts: the usual geostrophic  
425 scaled Laplace operator familiar from classical QG models, which will yield a smooth large-  
426 scale flow, and an acceleration term associated with advection by the background flow which is  
427 responsible for the generation of small-scale stationary waves. The boundary condition on (26) is  
428 no normal flow at the ridge. Since the flow is inviscid, an equivalent condition is that the ridge

429 is an isopycnal surface; that is, the net buoyancy  $B = b + N^2 z = 0$  at  $z = h(x)$  or the perturbation  
 430 buoyancy is  $b(z = h(x)) = -N^2 h(x)$ . In the linearized model (valid for small ridge heights) the  
 431 boundary condition is applied at  $z = 0$ , and the solution (e.g. Queney 1947; Pierrehumbert 1984)  
 432 is defined by the convolution

$$b(x, z) = -N^2 \int_{-\infty}^{\infty} G_L(x - x_0, z) h(x_0) dx_0, \quad (27)$$

433 where the Fourier transform of the Green's function  $G_L$  is

$$\widehat{G}_L(k, z) = \begin{cases} \exp \frac{iNkz}{\sqrt{k^2 U_0^2 - f^2}} & k > \frac{f}{U_0} \\ \exp \frac{-Nk|z|}{\sqrt{f^2 - k^2 U_0^2}} & 0 \leq k \leq \frac{f}{U_0} \end{cases}. \quad (28)$$

434 As with the equation (26), the steady solution is thus composed of two parts: a large-scale com-  
 435 ponent that decays with height, and a short-scale wave component that does not. These waves  
 436 are generated when the background flow is deflected (or accelerated) sufficiently rapidly over the  
 437 ridge into the stratified ambient, which provides a restoring force. Waves can only propagate for  
 438 Lagrangian frequencies exceeding  $f$  and *strong* wave generation only occurs when the acceleration  
 439 (or advective) timescale of  $1/(kU_0)$  is of this order,  $1/(kU_0) \sim 1/f$ , or equivalently the Rossby  
 440 number is order one,  $Ro_L = U_0/(fL) \sim 1$ . If the ridge is wide or the flow weak such that  $Ro_L \ll 1$ ,  
 441 then there is no significant wave field and flow remains in linearized, uniform PV geostrophic  
 442 balance, defined by  $\widehat{G}_L(k, z) = \exp(-Nk|z|/f)$ .

443 Let us now compare the dynamics of lee waves, as described in the previous paragraph, to the  
 444 dynamics of the strained front considered in earlier sections. To make the analogy clearer, here we  
 445 write the governing equation for a strained front with uniform interior PV ( $q_0 = 0$ ). This equation  
 446 is (9) with  $N^2$  constant and frontal anomaly  $b_0$  independent of  $z$ , or

$$\left[ \underbrace{(\bar{D}^2 - 2\alpha\bar{D} + f^2)}_{accel.} \underbrace{\frac{1}{N^2} \frac{\partial^2}{\partial z^2} + \frac{\partial^2}{\partial x^2}}_{geostrophic} \right] b = 0, \quad (29)$$

447 subject to boundary condition  $b = b_0(xe^{\alpha t})$ . Equation (29) describing a strained front is identical  
 448 in structure to (26) describing flow over a ridge — only the form of the acceleration terms differ.  
 449 The forced solution to (29) is defined by the convolution

$$b(x, z, t) = \int_{-\infty}^{\infty} G_F(x - x_0, z) b_0(xe^{\alpha t}) dx_0, \quad (30)$$

450 where the Green's function  $G_F$  may be determined via Fourier inversion of the Green's function  
 451  $G$  defined in (13). Unlike lee waves, where the ridge is rigid, the front deforms (sharpen) with  
 452 time as defined by the  $b_0(xe^{\alpha t})$  in (30). However, the solution for a particular frontal width at  
 453 some instant in time may be directly compared to the steady lee-wave solution for a ridge of the  
 454 same width. As for lee waves, this solution can be considered to be composed of two parts: a  
 455 large-scale secondary circulation or 'deflection' about the front, and a smaller-scale wave field.  
 456 Unfortunately, unlike the lee waves, the two parts are not readily separable. As was shown in  
 457 §2a2, if the strain rate  $\delta = \alpha/f \ll 1$  — analogous to  $Ro_L \ll 1$  for the lee waves — then there  
 458 is negligible generation of waves, and the flow reduces to geostrophic balance with  $G$  defined  
 459 by (19). Notably, in this small Rossby number limit, the topographic Green's function is the  
 460 identical to the frontal Green's function,  $\widehat{G}_F = \widehat{G}_L = \exp(-Nk|z|/f)$ . Comparing (27) and (30)  
 461 thus implies that the geostrophic buoyancy field associated with a topographic ridge of profile  
 462  $h(x)$  is identical to the geostrophic buoyancy field associated with a front with surface buoyancy  
 463 profile  $b_0(x) = -N^2h(x)$  at some instant in time. The secondary circulation around the front/ridge  
 464 is determined by material conservation of the buoyancy,  $w = -\bar{D}b/N^2$ , and so will be different for  
 465 the front and ridge owing to the different material derivative operator  $\bar{D}$ . However, in both cases  
 466 the secondary flow is generated owing to the need for the far-field horizontal flow to be deflected  
 467 along isopycnals and around the surface obstacle. If this deflection is sufficiently sharp/fast (i.e.  
 468  $Ro_L, \delta$  non-small) then buoyant forces give rise to a wave response.

### 469 3. Numerical model comparison

470 Here we describe a solution to the fully non-linear equations (3) for parameter values represen-  
471 tative of a submesoscale front. We consider a front with an initial structure of

$$b(x, z, 0) = \frac{\Delta b}{2} \left( 1 + \operatorname{erf} \left( \frac{x}{L} \right) \right) \exp \left( - \left( \frac{z}{H} \right)^2 \right) + N^2 z, \quad (31)$$

472 and choose a buoyancy difference of  $\Delta b = 5 \times 10^{-3} m^2 s^{-1}$ , initial frontal width of  $L = 10 km$ ,  
473 depth scale of  $H = 100 m$ , stratification  $N^2 = 1 \times 10^{-5} s^{-1}$  and assume  $f = 1 \times 10^{-4} s^{-1}$ . These  
474 parameters correspond to an initial geostrophic Rossby number — the parameter assumed to be  
475 small in the linear model — of  $Ro_g = \Delta b H / (f^2 L^2) = 0.5$ , although  $Ro_g$  increases to  $O(10)$  as the  
476 front sharpens. To prevent the generation of waves associated with the adjustment of unbalanced  
477 initial conditions, we initialise the numerical model with zero strain flow in a state of geostrophic  
478 balance and gradually ramp-up the strain rate with time according to  $\alpha(t) = \alpha_0 (1 - \exp -(t/\tau)^2)$ .  
479 Here we select a maximum strain rate of  $\alpha_0 = 0.4f$  and ramp-up timescale of  $\tau = 2\pi/f$ .

480 The numerical model employed is MITgcm (Marshall et al. 1997) configured in hydrostatic,  
481 two-dimensional, ocean-only mode with a rigid-lid ocean surface. The MITgcm code is modified  
482 to include the background strain advection terms in (3) as an external forcing in the buoyancy and  
483 horizontal momentum equations. The domain width is chosen as  $200 km$  with the front in the centre  
484 of the domain and a horizontal resolution of  $100 m$  at the front. Open boundaries with Orlandi  
485 radiation conditions are used at the horizontal edges of the domain. The domain depth is set to  $8 km$   
486 with resolution varying from  $5 m$  at the surface to  $25 m$  at depth. A uniform background horizontal  
487 diffusivity and viscosity of  $10 m^2 s^{-1}$  is introduced to prevent the collapse of the front below the  
488 grid-scale. We also add a diffusive sponge in the deep which absorbs downward propagating waves  
489 and prevents reflections off the base of the domain. The sponge takes the form of an elevated

490 diffusivity and viscosity in the bottom half of the domain,  $\kappa_h(z) = \kappa_\infty(1 + \text{erf}(-(z + 6)/1.5))/2$   
 491 where  $\kappa_\infty = 400 m^2 s^{-1}$  and  $z$  is in units of kilometers.

492 The numerical model ultimately reaches a steady state where strain-driven sharpening of the  
 493 front is balanced by the explicit horizontal diffusion. The time evolution of the model's surface  
 494 buoyancy field towards this steady state is shown in figure 6. The magnitude of the strain rate as  
 495 a function of time is also shown. As the front sharpens it moves to the left, with warmer fluid  
 496 slumping over cooler. The front reaches a steady state after about two days with a steady cross-  
 497 frontal width of about  $700 m$ . The vertical velocity field in the steady state is shown in figure 7a.  
 498 The grey lines on the figure are the wave and jet slopes predicted from the Green's function derived  
 499 in the previous section. These predicted slopes show good agreement with the numerical solution.

500 For comparison, the vertical velocity field predicted from the analytical model is shown in figure  
 501 7b. This prediction is derived in the following way. First, the frontal anomaly  $b_0$  is determined  
 502 from the initial buoyancy field  $b(x, z, 0)$  used in the numerical model (31). This is done by replac-  
 503 ing the velocity  $v$  in the PV relation (7) with the geostrophic velocity from (15) (since the model  
 504 is initialised in geostrophic balance) and rearranging to obtain,

$$b_0 = b - b' = b + \left(\frac{N}{f}\right)^2 \int \int \frac{\partial^2 b}{\partial x^2} dz dz. \quad (32)$$

505 In the absence of diffusion the frontal anomaly would sharpen continuously in time according to  
 506  $b_0(x e^{\beta(t)}, z)$  as discussed previously (where  $\beta(t) = \int_0^t \alpha(t') dt'$ ). The inclusion of diffusion will  
 507 limit the sharpening of the front to a finite width. To determine this width, consider that at steady  
 508 state the dominant balance is between the strain and diffusion, or  $-\alpha x \partial_x b \simeq \kappa_h \partial_{xx} b$ , which may  
 509 be solved to obtain  $b(x) = \Delta b (1 + \text{erf}(x/L_s))/2$  where the width of the front is  $L_s = \sqrt{2\kappa_h/\alpha}$   
 510 (Shakespeare and Taylor 2015). For the present values the steady frontal width is  $L_s = 707 m$   
 511 in agreement with figure 6. Thus, the frontal anomaly  $b_0$  will approach  $b_0(xL_0/L_s, z)$  at large

512 time, where  $L_0$  is the initial frontal width. This frontal anomaly is convolved with the Green's  
513 function to determine the analytical vertical velocity field shown in figure 7b. The waves seen  
514 in this solution compare well in both structure and amplitude with those in the numerical model  
515 solution, particularly at depth.

516 The region where the linear model is expected to break down may be computed by considering  
517 the linearization assumption,  $|u| \ll |\bar{U}|$ , made in the model derivation. The edge of this region  
518 approximately corresponds to the line along which  $|u| = 0.1|\bar{U}|$  (solid black curve on figure 7) as  
519 derived from the analytic solution. Indeed, the major differences between the numerical and ana-  
520 lytical solutions occur near the surface front within this contour, where the secondary circulation  
521 (i.e.  $u$ ) and local Rossby number are large. Figure 8 shows a magnified view of the steady solu-  
522 tions near the surface front. The local vorticity Rossby number,  $Ro = f^{-1} \partial_x v$ , from the numerical  
523 model (figure 8a) peaks at a value of 7.9 at the surface front. Associated with this large Rossby  
524 number, the surface front in the numerical solution (figure 8b) has slumped to the left under the  
525 influence of gravity. This slumping has the effect of stabilizing the isopycnals compared to the an-  
526 alytic solution (figure 8c), which is gravitationally unstable near the surface. Associated with the  
527 non-linear leftward slumping of the front, the numerical vertical velocity (figure 8b) is weakened  
528 on the warm (cyclonic; right) side of the front, and strengthened on the cool (anticyclonic; left)  
529 side, relative to the analytic solution. The numerical solution also exhibits an intense downward  
530 jet on the cool side of the front, not present in the analytic solution. Similarly, the first few lowest  
531 Lagrangian frequency waves on the cool side of the front are intensified and steepened directly  
532 below the surface front. Furthermore, in the numerical solution the first (lowest frequency) wave  
533 mode appears on the cool side of the front around  $t = 20$  hours, whereas the corresponding wave  
534 mode on the warm side of the front only appears later, around  $t = 25$  hours. This behavior contrasts  
535 with the perfect antisymmetry maintained by the linearized analytic solution.

536 Some of the non-linear dynamics associated with the surface front in the numerical solution can  
 537 be described by non-linear frontal models (e.g. Hoskins and Bretherton 1972; Shakespeare and  
 538 Taylor 2014) which use the momentum coordinate,  $X = x + v/f$ , to include the effect of non-  
 539 linear cross-frontal advection (i.e.  $u \partial_x$ ). The buoyancy  $b$  in the non-linear models is described  
 540 by the same equation as in the linear models, but in the transformed coordinate — that is, with  $x$   
 541 in (9) replaced by  $X$  (Shakespeare 2015a). In other words, non-linear models of two-dimensional  
 542 fronts differ from linear models by the translation  $x = X - v(X, z, t)/f$  of the solution, where  $X$  is  
 543 the coordinate appearing in the linear solution. The *magnitude* of the along-front flow  $v$  does not  
 544 change. However, the coordinate contraction associated with the translation  $x = X - v(X, z, t)/f$   
 545 does imply an amplification of the cross-frontal flow (i.e.  $u, w$ ) to conserve volume. In particular,  
 546 the vertical velocity in the non-linear solution is scaled by the absolute vorticity,  $\zeta/f = (1 +$   
 547  $f^{-1} \partial_x v) = (1 - f^{-1} \partial_X v)^{-1}$ , relative to the linear solution. We note that this relationship between  
 548 linear and non-linear models has only been shown to be valid for the case of uniform interior  
 549 PV, whereas here we have a variable PV. Nonetheless, here we apply these transformations to the  
 550 linear model solution shown in figure 8c to obtain the ad-hoc non-linear solution shown in 8d.  
 551 The ad-hoc solution captures some features of the fully non-linear numerical solution such as the  
 552 location of the surface front and asymmetry of the vertical velocity field. However, as a result of  
 553 the very large Rossby number at the front, the ad-hoc solution also exhibits a discontinuity in the  
 554 buoyancy field at the surface front (down to a depth of about 40m) and an associated infinity in  
 555 the vertical velocity, implying that diffusion and other non-linear effects are important in arresting  
 556 the collapse of the surface front. These large Rossby number dynamics are discussed in detail in  
 557 Shakespeare and Taylor (2015).

558 *a. Wave propagation and frequency spectra*

559 As seen in previous sections, the spontaneously generated waves are horizontally trapped by the  
 560 strain flow and rapidly become steady in the numerical solution (e.g. figure 7). This behavior is  
 561 due to spatially uniform strain flow, and thus differs from what would be expected in the ocean  
 562 where strain flows vary greatly in space (both horizontally and vertically). While we cannot di-  
 563 rectly represent such spatial variability in our simple quasi-2D model, we can capture some of the  
 564 dynamics by considering a temporal variation in the spatially-uniform strain rate. In particular,  
 565 here we consider switching off the strain flow in the steady numerical solutions described in the  
 566 previous section (§3). As the strain rate is reduced, the trapped stationary waves are able to prop-  
 567 agate, consistent with observations of waves at ocean fronts (e.g. Alford et al. 2013), and we can  
 568 analyze the frequency spectrum of the flow and compare to our analytic predictions.

569 The methodology is as follows. We take the steady numerical solution (figure 7a) from the  
 570 previous section and at time  $t = 60$  hours switch off the strain flow in two ways: (a) instantaneously  
 571 such that

$$\alpha(t) = \begin{cases} \alpha_0 \left(1 - e^{-\left(\frac{t}{\tau}\right)^2}\right) & t \leq 60 \\ 0 & t > 60 \end{cases}, \quad (33)$$

572 and (b) gradually over 60 hours such that

$$\alpha(t) = \begin{cases} \alpha_0 \left(1 - e^{-\left(\frac{t}{\tau}\right)^2}\right) & t \leq 60 \\ \alpha_0 \left(1 - e^{-\left(\frac{120-t}{\tau}\right)^2}\right) & 60 < t \leq 120 \\ 0 & t > 120 \end{cases}, \quad (34)$$

573 where time is in hours and the parameter values are the same as previously (i.e.  $\tau = 2\pi/f$ ,  $\alpha_0 =$   
 574  $0.4f$ ). The frequency spectrum of the vertical velocity field,  $|\widehat{w}|(x, z, \omega)$ , in each case is then  
 575 analyzed for a period of 120 hours from when the strain rate reaches zero (this approach avoids

576 any Doppler shifting of the frequency due to non-zero background flow, e.g. (22e)). Here we will  
 577 consider the spatially averaged vertical velocity spectrum (units:  $m$ ) defined by

$$\langle |\widehat{w}| \rangle = \frac{\int \int |\widehat{w}| dx dz}{\int \int dx dz}. \quad (35)$$

578 The spectrum  $\langle |\widehat{w}| \rangle$  is plotted in figure 9 for the (a) instantaneous and (b) gradual strain switch-  
 579 off. Three spectra are shown in each plot: the average over the whole numerical domain (solid), the  
 580 average above  $50m$  (dashed), and the average below  $4km$  (dotted). The global average in figure 9a  
 581 shows three distinct spectral peaks coincident with the frequencies corresponding to the secondary  
 582 circulation (vertical line labelled B), and the first two wave modes (vertical lines labelled C and D)  
 583 for a strain rate of  $0.4f$  as derived from figures 3 and 4. Thus, unsurprisingly, once the strain flow  
 584 is switched off, the previously stationary wave modes begin to propagate at the frequency set by  
 585 their slopes. The first wave mode (C) is particularly evident. Perhaps less expected is the strong  
 586 wave generation corresponding to what we previously identified as the secondary circulation or  
 587 frontal jets (line B; global spectra). This wave generation is associated with the ‘adjustment’ of the  
 588 secondary circulation — that is, once the strain rate becomes zero, a steady secondary circulation  
 589 cannot be supported at the front, and the excess momentum (sometimes called a ‘momentum  
 590 imbalance’) is removed via the generation of inertia gravity waves. This adjustment generation  
 591 has previously been examined in various contexts by many authors (e.g. Rossby 1938; Blumen  
 592 2000; Shakespeare and Taylor 2013, 2015). These adjustment waves would be generated even in  
 593 the limit of very weak strain rate, if the strain field is turned off instantaneously, in contrast to the  
 594 identified wave modes (C, D), which would vanish in this limit.

595 Now instead consider frequency spectrum associated with the gradual switch-off plotted in figure  
 596 9b. The gradual variation of the strain rate ensures that there is no instantaneous adjustment  
 597 process, and the spectral peak associated with the secondary circulation is no longer present. In

598 addition, instead of distinct spectral peaks corresponding to individual wave modes (lines C, D),  
 599 there is a broad band of high frequency wave energy which peaks around  $2f$ . The reason for  
 600 this is that as the strain rate varies the resonant wave mode frequencies (e.g. figure 4) change,  
 601 such that waves of different frequencies are continually being generated via the acceleration of the  
 602 strain flow around the front. Notably, the peak spectral amplitude still occurs around  $2f$  which  
 603 agrees with the lowest frequency (highest amplitude) wave mode for strain rates in the range  
 604  $0.25 < \alpha/f < 0.4$  (see figure 4). The globally averaged spectrum in figure 9b also exhibits a peak  
 605 at the inertial frequency (line A) associated with direct forcing from the time-varying strain rate  
 606 which itself varies near-inertially (e.g. (34)).

#### 607 4. Discussion

608 Here we have investigated the spontaneous generation of inertia-gravity waves at strongly  
 609 strained density fronts. In §2a we developed a linearized model to derive solutions for the cir-  
 610 culation and density fields associated with a background strain flow,  $\bar{U} = -\alpha x$ , acting across a  
 611 frontal buoyancy anomaly in a semi-infinite domain. The solutions depend only on the magnitude  
 612 of the strain rate and the structure of the frontal anomaly,  $b_0(x, z)$ , at some instant in time. All  
 613 information about the amplitude and structure of the frontal circulation, and Lagrangian wave fre-  
 614 quencies, is contained with the Green's function for the problem (see figure 1). Whether waves  
 615 are generated at a given front is determined by the Burger number of the front and the strain rate.  
 616 Here we define the Burger number as  $\varepsilon_F = NH/(fL)$ , where  $H$  is the depth of the frontal structure,  
 617  $L$  the width, and  $N/f$  the ratio of buoyancy to inertial frequencies. Wave generation is predicted  
 618 for Burger numbers exceeding about 0.5 and strain rates,  $\alpha$ , exceeding about  $0.2f$ . The lowest  
 619 frequency distinct wave predicted to be generated by the present mechanism has Lagrangian fre-  
 620 quency  $\omega = 1.93f$  and is generated for a strain rate of  $\alpha = 0.29f$  (see figure 4). Based on these

621 results, it seems unlikely that the mechanism of wave generation examined here was responsible  
622 for the front-sourced waves observed by Alford et al. (2013) which were of very low frequency  
623 ( $\sim 1.01f$ ). Wave amplitudes increase with increasing frontal Burger number and background  
624 strain rate.

625 We also investigated the mechanism responsible for the generation of the frontal waves. In §2b  
626 we showed that wave generation at a strained front is mathematically analogous to the classical  
627 scenario of ‘lee wave’ generation associated with a uniform flow over a topographic ridge in a  
628 rotating system (e.g. Queney 1947). Waves are generated in each case whenever the acceleration  
629 of the background flow around the front/ridge into the stratified ambient is fast enough that it forces  
630 the system away from geostrophic balance. More generally, any structure that presents an obstacle  
631 to the background strain flow will tend to generate waves, not only surface density fronts. Indeed,  
632 the analytic solution implies that any surface or interior PV anomaly  $q_0$  (i.e. equation (5)) with  
633 some horizontal structure, whether in a bounded or unbounded domain, will generate waves in a  
634 strain flow. This result appears to be closely related to that of recent analytical studies describing  
635 the generation of gravity waves by a PV anomaly in a *shear* flow (Lott et al. 2010, 2012). These  
636 studies also employed a similar analytic approach using linearized equations of motion.

637 The present model is intended as a first-order description of wave generation in regions of the  
638 ocean with both sharp horizontal buoyancy gradients (order one frontal Burger numbers) and  
639 strong strain flows, such as the ocean submesoscale. Based on the analytic model results, we  
640 anticipate strong wave generation at submesoscale fronts. However, submesoscale fronts also typ-  
641 ically exhibit large vorticity and Rossby number — a parameter that is assumed to be small in  
642 the linearized analytical model. Despite this assumption, in §3 we showed that the wave field  
643 in the analytic solution compares well with a fully non-linear numerical solution to the problem  
644 (i.e. equations (3)) for parameter values representative of a submesoscale front. The solutions

645 only differ significantly near the surface front, with the numerical solution developing an intense  
646 downward jet on the cooler side of the front. The shallowest slope waves on the cooler side of  
647 the front are also intensified relative to the analytic prediction, and tend to appear earlier than  
648 their counterparts on the warm side. Given these relatively minor differences, we can be confident  
649 that the analytic model provides a robust, first-order dynamical description of one mechanism of  
650 inertia-gravity wave generation at strained density fronts.

651 However, more investigation is needed in more realistic models to quantify the relative impor-  
652 tance of spontaneous generation at strained density fronts to the global wave field. The model  
653 used herein is highly idealized, describing a two-dimensional front subject to a spatially uniform  
654 background strain flow. These assumptions will almost certainly break down on the submesoscale  
655 where both the background strain flows and the density fronts are highly three-dimensional in  
656 character, and evolve on super-inertial timescales. For example, Nagai et al. (2015) use a high  
657 resolution numerical model to show that spontaneously generated waves at fronts can be reabsorbed  
658 by the mean flow, rather than propagating away as described by our model. More realistic spatial  
659 and temporal variability will also likely modify the amplitude and frequencies of generated waves  
660 compared to our analytic predictions. These effects will be studied in a future work.

661 *Acknowledgments.* CJS was supported by a Gates Cambridge Scholarship.

## 662 **References**

663 Alford, M. H., A. Y. Shcherbina, and M. C. Gregg, 2013: Observations of near-inertial internal  
664 gravity waves radiating from a frontal jet. *J. Phys. Oceanogr.*, **43**, 1225–1239.

665 Blumen, W., 2000: Inertial oscillations and frontogenesis in a zero potential vorticity model. *J.*  
666 *Phys. Oceanogr.*, **30**, 31–39.

- 667 Booker, J. R., and F. P. Bretherton, 1967: The critical layer for internal gravity waves in a shear  
668 flow. *J. Fluid Mech.*, **27** (03), 513–539.
- 669 Capet, X., J. C. McWilliams, M. J. Molemaker, and A. F. Shchepetkin, 2008: Mesoscale to  
670 submesoscale transition in the California Current system. Part II: Frontal processes. *J. Phys.*  
671 *Oceanogr.*, **38**, 44–64.
- 672 Danioux, E., J. Vanneste, P. Klein, and H. Sasaki, 2012: Spontaneous inertia-gravity-wave gener-  
673 ation by surface-intensified turbulence. *J. Fluid Mech.*, **699**, 153–1732.
- 674 D’Asaro, E., C. Lee, L. Rainville, R. Harcourt, and L. Thomas, 2011: Enhanced turbulence and  
675 energy dissipation at ocean fronts. *Science*, **332** (6027), 318–322.
- 676 Ford, R., 1994: The instability of an axisymmetric vortex with monotonic potential vorticity in  
677 rotating shallow water. *J. Fluid Mech.*, **280**, 303–334.
- 678 Gill, A. E., 1984: On the behavior of internal waves in the wakes of storms. *J. Phys. Oceanogr.*,  
679 **14** (7), 1129–1151.
- 680 Griffiths, M., and M. J. Reeder, 1996: Stratospheric inertia-gravity waves generated in a numerical  
681 model of frontogenesis. I: Model solutions. *Q. J. Roy. Meteor. Soc.*, **122**, 1153–1174.
- 682 Gula, J., M. J. Molemaker, and J. C. McWilliams, 2014: Submesoscale cold filaments in the Gulf  
683 Stream. *J. Phys. Oceanogr.*, **44** (10), 2617–2643.
- 684 Hosegood, P. J., M. C. Gregg, and M. H. Alford, 2013: Wind-driven submesoscale subduction at  
685 the north Pacific subtropical front. *J. Geophys. Res.*, **118** (10), 5333–5352.
- 686 Hoskins, B. J., and F. P. Bretherton, 1972: Atmospheric frontogenesis models: mathematical  
687 formulation and solution. *J. Atmos. Sci.*, **29**, 11–37.

- 688 Kunze, E., 1985: Near-inertial wave propagation in geostrophic shear. *Journal of Physical*  
689 *Oceanography*, **15** (5), 544–565.
- 690 Lott, F., R. Plougonven, and J. Vanneste, 2010: Gravity waves generated by sheared potential  
691 vorticity anomalies. *J. Atmos. Sci.*, **67** (1), 157–170.
- 692 Lott, F., R. Plougonven, and J. Vanneste, 2012: Gravity waves generated by sheared three-  
693 dimensional potential vorticity anomalies. *J. Atmos. Sci.*, **69** (7), 2134–2151.
- 694 Mahadevan, A., and A. Tandon, 2006: An analysis of the mechanisms for submesoscale vertical  
695 motion at ocean fronts. *Ocean Modell.*, **14**, 241–256.
- 696 Marshall, J., A. Adcroft, C. Hill, L. Perelman, and C. Heisey, 1997: A finite-volume, incom-  
697 pressible Navier Stokes model for studies of the ocean on parallel computers. *J. Geophys. Res.*,  
698 **102** (C3), 5753–5766.
- 699 Muraki, D. J., 2011: Large-amplitude topographic waves in 2D stratified flow. *J. Fluid Mech.*,  
700 **681**, 173–192.
- 701 Nagai, T., A. Tandon, E. Kunze, and A. Mahadevan, 2015: Spontaneous generation of near-inertial  
702 waves by the Kuroshio Front. *J. Phys. Oceanogr.*, **45** (9), 2381–2406.
- 703 Pierrehumbert, R. T., 1984: Linear results on the barrier effects of mesoscale mountains. *J. Atmos.*  
704 *Sci.*, **41** (8), 1356–1367.
- 705 Plougonven, R., and C. Snyder, 2005: Gravity waves excited by jets: propagation versus genera-  
706 tion. *Geophys. Res. Lett.*, **32**, doi:10.1029/2005GL023730.
- 707 Plougonven, R., and F. Zhang, 2014: Internal gravity waves from atmospheric jets and fronts. *Rev.*  
708 *Geophys.*, **52** (1), 33–76.

- 709 Polzin, K. L., 2010: Mesoscale eddy-internal wave coupling. Part II: energetics and results from  
710 PolyMode. *J. Phys. Oceanogr.*, **40**, 789–801.
- 711 Polzin, K. L., and Y. V. Lvov, 2011: Toward regional characterizations of the oceanic internal  
712 wavefield. *Rev. Geophys.*, **49** (4).
- 713 Queney, P., 1947: *Theory of perturbations in stratified currents with applications to air flow over*  
714 *mountain barriers*. University of Chicago Press.
- 715 Reeder, M. J., and M. Griffiths, 1996: Stratospheric inertia-gravity waves generated in a numerical  
716 model of frontogenesis. II: Wave sources, generation mechanisms and momentum fluxes. *Q. J.*  
717 *Roy. Meteor. Soc.*, **122**, 1175–1195.
- 718 Rossby, C. G., 1938: On the mutual adjustment of pressure and velocity distributions in certain  
719 simple current systems, II. *J. Mar. Res.*, **1**, 239–263.
- 720 Rosso, I., A. M. Hogg, A. E. Kiss, and B. Gayen, 2015: Topographic influence on sub-  
721 mesoscale dynamics in the Southern Ocean. *Geophys. Res. Lett.*, **42** (4), 1139–1147, doi:  
722 10.1002/2014GL062720.
- 723 Rudnick, D. L., and J. R. Luyten, 1996: Intensive surveys of the Azores Front 1. Tracers and  
724 dynamics. *J. Geophys. Res.*, **101** (C1), 923–939.
- 725 Shakespeare, C. J., 2015a: Non-hydrostatic wave generation at strained fronts. *J. Atmos. Sci.*, **in**  
726 **press**.
- 727 Shakespeare, C. J., 2015b: On the generation of waves during frontogenesis. University of Cam-  
728 bridge.
- 729 Shakespeare, C. J., and J. R. Taylor, 2013: A generalized mathematical model of geostrophic  
730 adjustment and frontogenesis: uniform potential vorticity. *J. Fluid Mech.*, **736**, 366–413.

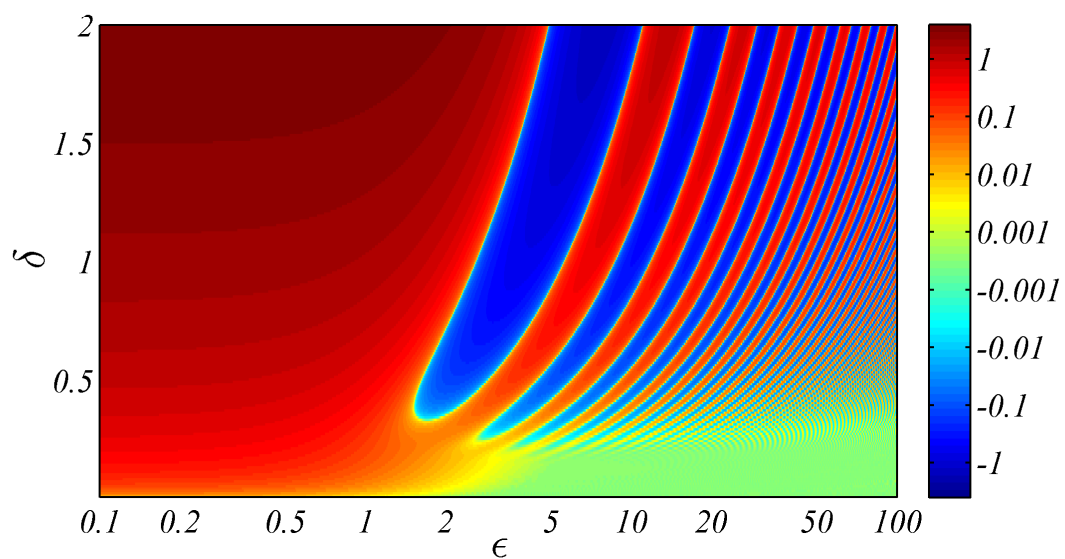
- 731 Shakespeare, C. J., and J. R. Taylor, 2014: The spontaneous generation of inertia-gravity waves  
732 during frontogenesis forced by large strain: theory. *J. Fluid Mech.*, **757**, 817–853.
- 733 Shakespeare, C. J., and J. R. Taylor, 2015: The spontaneous generation of inertia-gravity waves  
734 during frontogenesis forced by large strain: numerical solutions. *J. Fluid Mech.*, **accepted**.
- 735 Shcherbina, A. Y., E. A. D’Asaro, C. M. Lee, J. M. Klymak, M. J. Molemaker, and J. C.  
736 McWilliams, 2013: Statistics of vertical vorticity, divergence, and strain in a developed sub-  
737 mesoscale turbulence field. *Geophys. Res. Lett.*, **40**, doi:10.1002/grl.50919.
- 738 Snyder, C., W. Skamarock, and R. Rotunno, 1993: Frontal dynamics near and following frontal  
739 collapse. *J. Atmos. Sci.*, **50**, 3194–3211.
- 740 Thomas, L. N., 2012: On the effects of frontogenetic strain on symmetric instability and inertia-  
741 gravity waves. *J. Fluid Mech.*, **711**, 620–640.
- 742 Thomas, L. N., A. Tandon, and A. Mahadevan, 2008: Submesoscale processes and dynamics.  
743 *Geophysical Monograph Series 177: Ocean Modeling in an Eddying Regime*, American Geo-  
744 physical Union.
- 745 Vanneste, J., 2013: Balance and spontaneous wave generation in geophysical flows. *Annu. Rev.*  
746 *Fluid Mech.*, **45**, 147–172.
- 747 Viudez, A., and D. G. Dritschel, 2006: Spontaneous generation of inertia-gravity wave packets by  
748 balanced geophysical flows. *J. Fluid Mech.*, **553**, 107–117.
- 749 Whitt, D. B., and L. N. Thomas, 2013: Near-inertial waves in strongly baroclinic currents. *Journal*  
750 *of Physical Oceanography*, **43** (4), 706–725.
- 751 Williams, R. T., and J. Plotkin, 1968: Quasi-geostrophic frontogenesis. *J. Atmos. Sci.*, **25**, 201–  
752 206.

- 753 Wunsch, C., and R. Ferrari, 2004: Vertical mixing, energy and the general circulation of the  
754 oceans. *Annu. Rev. Fluid Mech.*, **36**, 281–314.
- 755 Zhang, F., 2004: Generation of mesoscale gravity waves in upper-tropospheric jet-front systems.  
756 *J. Atmos. Sci.*, **61**, 440–457.

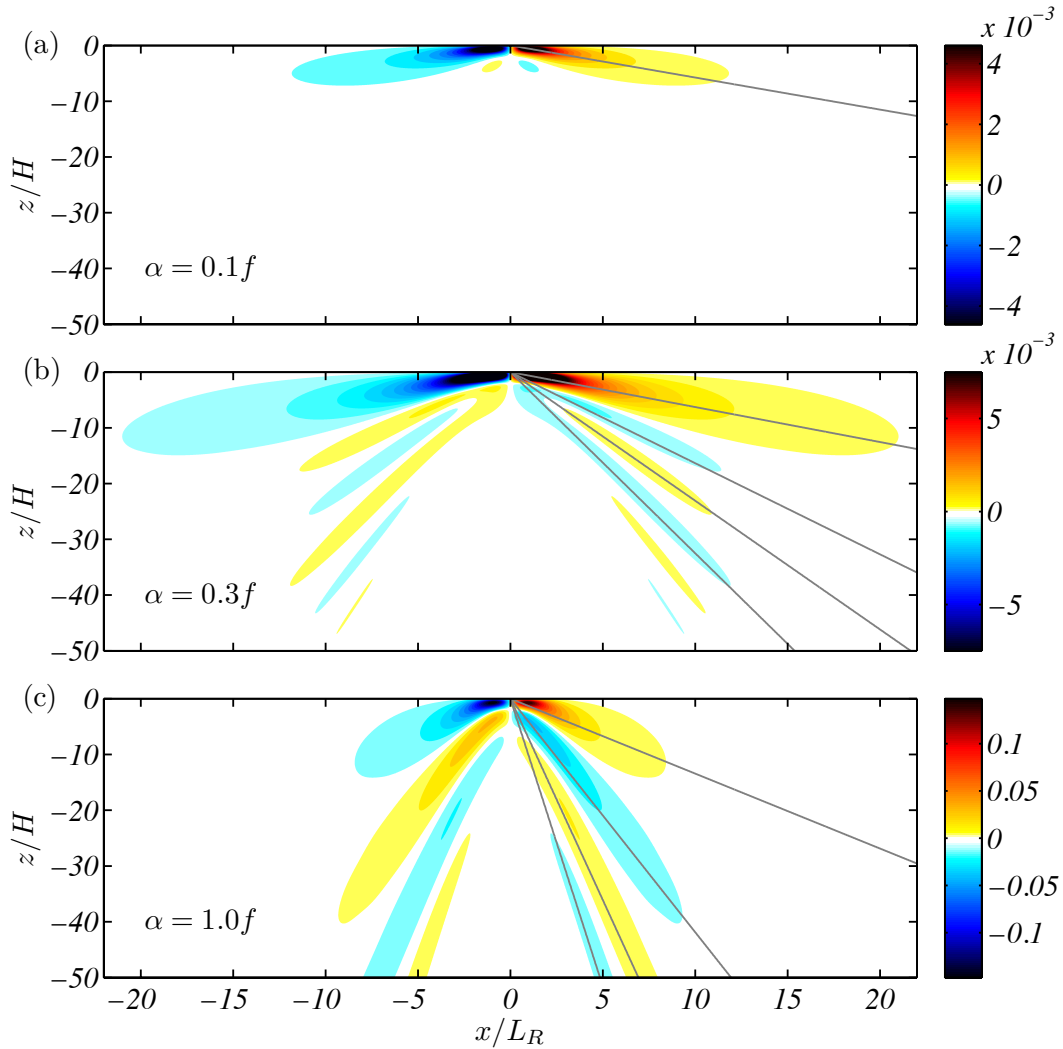
## LIST OF FIGURES

757		
758	<b>Fig. 1.</b>	Non-dimensional Green's function for the cross-front shear, $f \widehat{\partial_z u_G}$ (17), as a function of
759		slope $\varepsilon = Nk/(fm)$ and strain rate $\delta = \alpha/f$ . Local extrema in the Green's function corre-
760		spond to waves (resonant modes) with Lagrangian frequency $\omega = f\sqrt{1 + \varepsilon^2}$ . . . . . 40
761	<b>Fig. 2.</b>	Comparison of vertical velocity field (in units of $\Delta b_0 f/N^2$ ) for strain rates (a) $\alpha = 0.1f$ , (b)
762		$\alpha = 0.3f$ , and (c) $\alpha = f$ , and a frontal anomaly defined by (21). Straight grey lines indicate
763		the slopes of secondary circulation and first three wave modes (if they exist), as predicted
764		from the Green's function (see figures 3 and 4). . . . . 41
765	<b>Fig. 3.</b>	(a) Slope of the frontal jets as a function of strain rate, in units of $f/N$ . (b) Vertical velocity
766		magnitude as a function of strain rate, in units of $\Delta b_0 H/(NL)$ . The results from the small
767		(19) and large (20) strain rate limits are shown as dashed lines. The slope is nearly constant
768		at small strain rate and increases linearly at large strain rate. The vertical velocity increases
769		linearly at small strain rate and quadratically at large strain rate. . . . . 42
770	<b>Fig. 4.</b>	Frequencies of the six lowest frequency distinct wavepackets as a function of strain rate $\delta =$
771		$\alpha/f$ , derived from computing the local extrema of the non-dimensional cross-front shear
772		Green's function, $f \widehat{\partial_z u_G}$ , shown in figure 1. The lowest Lagrangian frequency associated
773		with a distinct wave mode is $\omega = 1.93f$ , for a strain rate of $\alpha = 0.29f$ . . . . . 43
774	<b>Fig. 5.</b>	Vertical velocity fields for a strain rate of $\alpha = 0.4f$ and buoyancy anomaly defined by (21),
775		for various frontal Burger numbers $\varepsilon_F = L_R/L$ . The velocities are in units of $\varepsilon_F \Delta b_0 f/N^2$ .
776		Contours are logarithmically spaced from 3 to 100% of the maximum value (0.03). Grey-
777		dashed lines indicate the predicted slope of the frontal jets and waves. The figure can also
778		be viewed as a sequence of snapshots in time, $\alpha t = \ln(\varepsilon_F/0.1)$ : (a) $\alpha t = 0$ , (b) $\alpha t = 0.69$ ,
779		(c) $\alpha t = 1.61$ , (d) $\alpha t = 2.30$ , and (e) $\alpha t = 3$ . The path of a wave packet initially located
780		at the origin at $t = 0$ , with initial wavenumbers $k_0 = 0.2/L_R$ and $m_0 = 0.5/H$ , is shown by
781		a solid black line on each plot. The terminus of the line is the position of the wave packet
782		at the time the snapshot is taken. Note that the velocities have been non-dimensionalised
783		by $\varepsilon_F \Delta b_0 f/N^2$ , such that the maximum velocity in (e) is 20 times that in (a) owing to the
784		change in $\varepsilon_F$ . . . . . 44
785	<b>Fig. 6.</b>	The time evolution of the strain rate, $\alpha(t)/f$ , and the surface buoyancy field, $b(x, 0, t)$ , in the
786		numerical model. A steady state is reached after about 45 hours. . . . . 45
787	<b>Fig. 7.</b>	Comparison of the numerical and analytical solutions. (a) The steady state numerical vertical
788		velocity ( $\text{m day}^{-1}$ ) field. (b) The analytical vertical velocity field ( $\text{m day}^{-1}$ ) for the same
789		frontal structure (see text for details). The grey lines on each plot are the wave and jet slopes
790		predicted from the Green's function. The region for which $ u  > 0.1 \bar{U} $ , where the analytical
791		model is expected to break down, is enclosed by a solid black line on each plot. . . . . 46
792	<b>Fig. 8.</b>	Comparison of the numerical and analytical solutions near the surface front. (a) The vorticity
793		Rossby number $Ro = f^{-1} \partial_x v$ in the numerical model steady state. (b) The vertical velocity
794		field ( $\text{m day}^{-1}$ ) and buoyancy contours in the numerical model steady state. (c) The vertical
795		velocity field ( $\text{m day}^{-1}$ ) and buoyancy contours predicted by the analytical model. (d) The
796		vertical velocity field ( $\text{m day}^{-1}$ ) and buoyancy contours of the ad-hoc non-linear analytical
797		model (see text for detailed description). . . . . 47
798	<b>Fig. 9.</b>	Spatially averaged vertical velocity frequency spectra $\langle \widehat{ w } \rangle$ ( $\text{m}$ ) from the numerical solution
799		when the strain is turned off (a) instantaneously (33) and (b) gradually (34). Three lines are
800		displayed on each plot for the global average spectrum (solid), near-surface spectrum (above

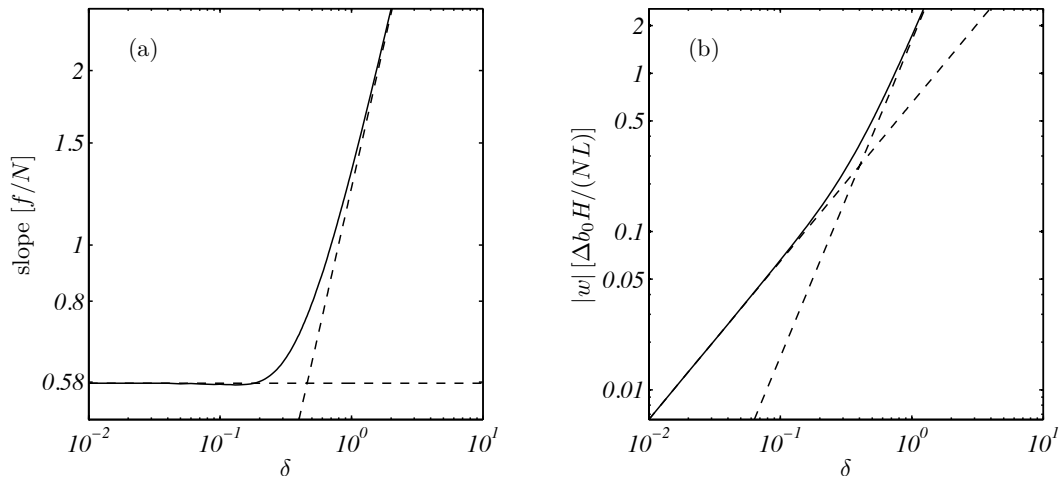
801 50m, dash) and deep spectrum (below 4km, dotted). The vertical grey lines labelled A to D  
802 indicate the specific frequencies of interest: A = inertial frequency, B = secondary circula-  
803 tion 'frequency', C = first wave mode frequency, and D = second wave mode frequency, as  
804 predicted from the constant strain analytic model for a strain rate of  $\alpha = 0.4f$ . . . . . 48



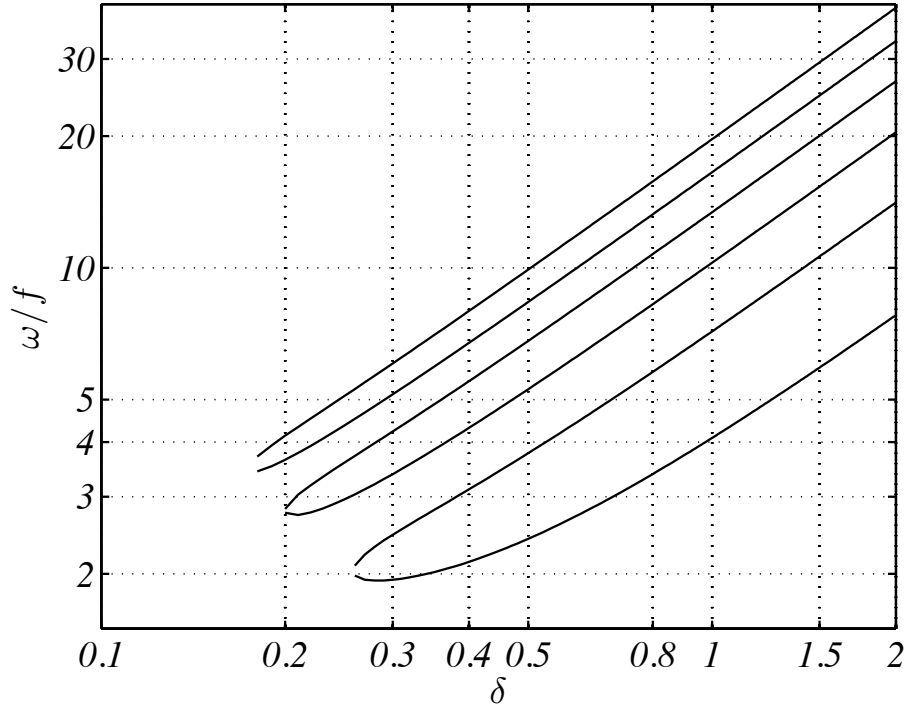
805 FIG. 1. Non-dimensional Green's function for the cross-front shear,  $f \widehat{\partial_z u_G}$  (17), as a function of slope  $\epsilon =$   
 806  $Nk/(fm)$  and strain rate  $\delta = \alpha/f$ . Local extrema in the Green's function correspond to waves (resonant modes)  
 807 with Lagrangian frequency  $\omega = f\sqrt{1 + \epsilon^2}$ .



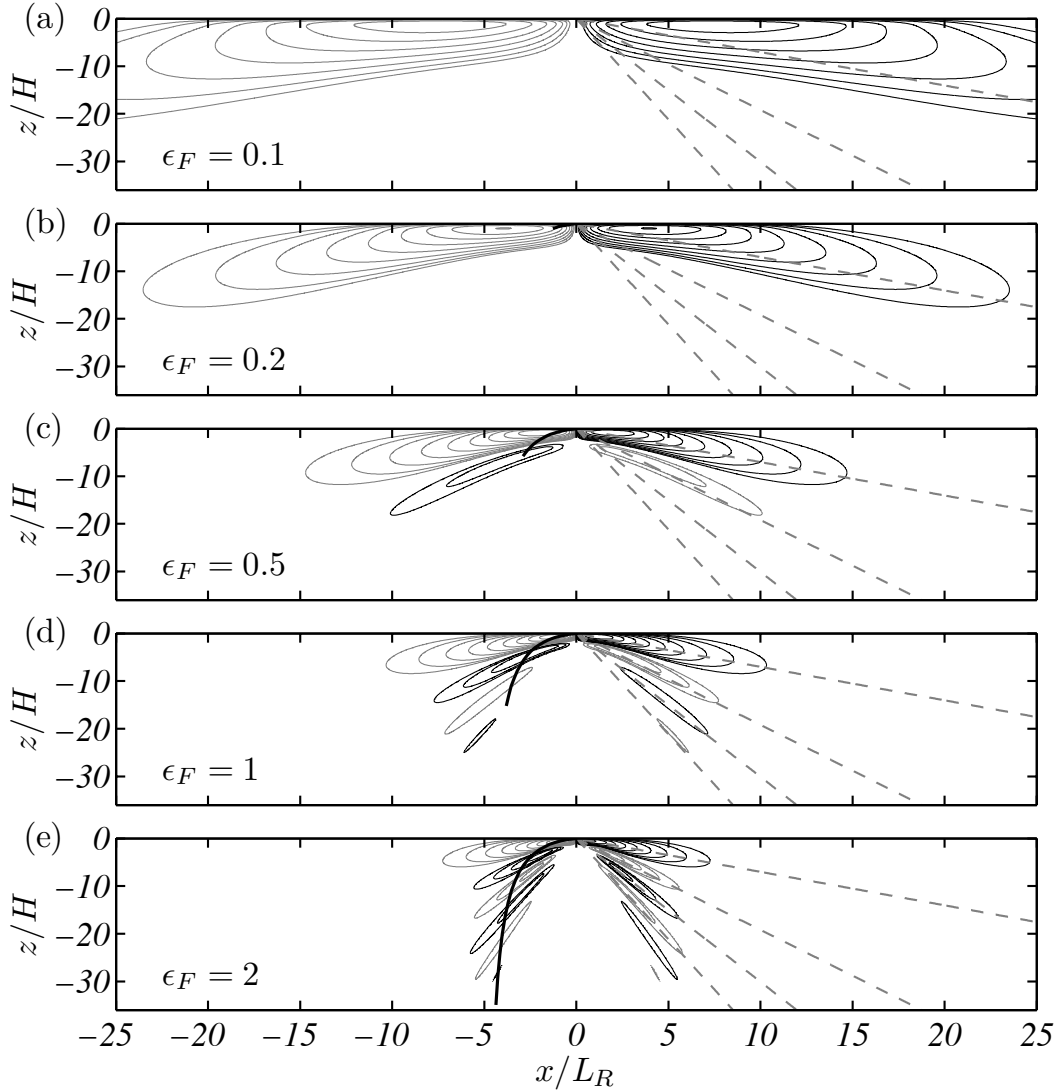
808 FIG. 2. Comparison of vertical velocity field (in units of  $\Delta b_0 f / N^2$ ) for strain rates (a)  $\alpha = 0.1f$ , (b)  $\alpha = 0.3f$ ,  
 809 and (c)  $\alpha = f$ , and a frontal anomaly defined by (21). Straight grey lines indicate the slopes of secondary  
 810 circulation and first three wave modes (if they exist), as predicted from the Green's function (see figures 3 and  
 811 4).



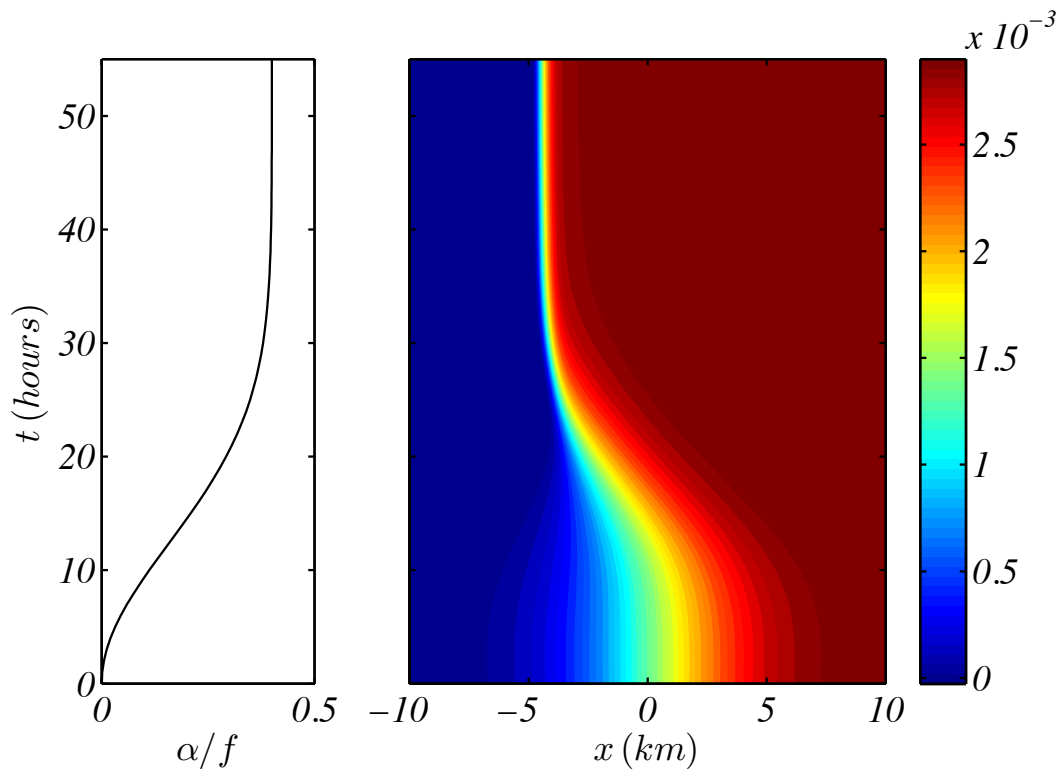
812 FIG. 3. (a) Slope of the frontal jets as a function of strain rate, in units of  $f/N$ . (b) Vertical velocity magnitude  
 813 as a function of strain rate, in units of  $\Delta b_0 H / (NL)$ . The results from the small (19) and large (20) strain rate  
 814 limits are shown as dashed lines. The slope is nearly constant at small strain rate and increases linearly at large  
 815 strain rate. The vertical velocity increases linearly at small strain rate and quadratically at large strain rate.



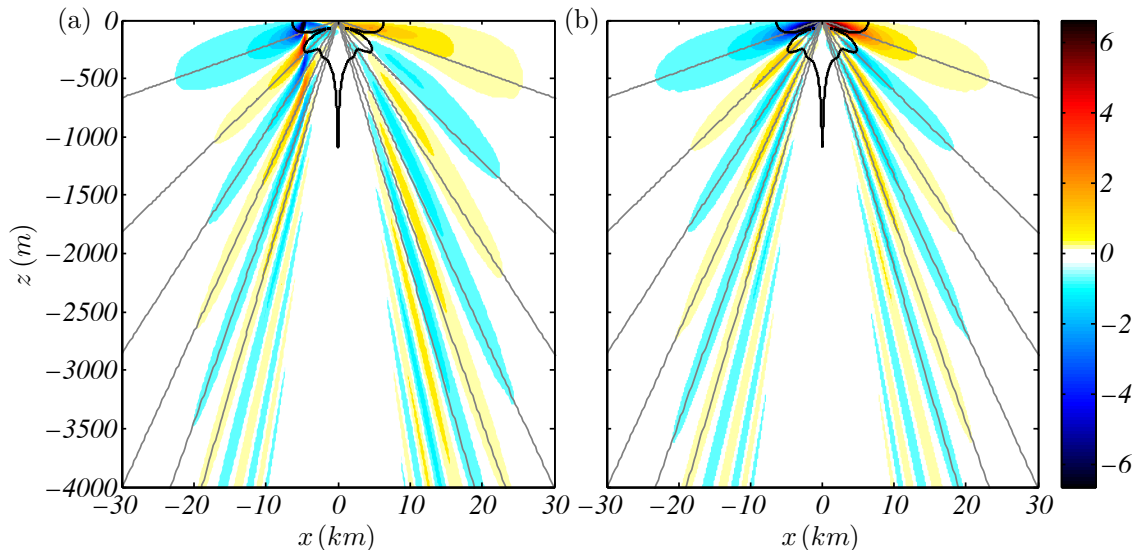
816 FIG. 4. Frequencies of the six lowest frequency distinct wavepackets as a function of strain rate  $\delta = \alpha/f$ ,  
 817 derived from computing the local extrema of the non-dimensional cross-front shear Green's function,  $f\widehat{\partial_z u_G}$ ,  
 818 shown in figure 1. The lowest Lagrangian frequency associated with a distinct wave mode is  $\omega = 1.93f$ , for a  
 819 strain rate of  $\alpha = 0.29f$ .



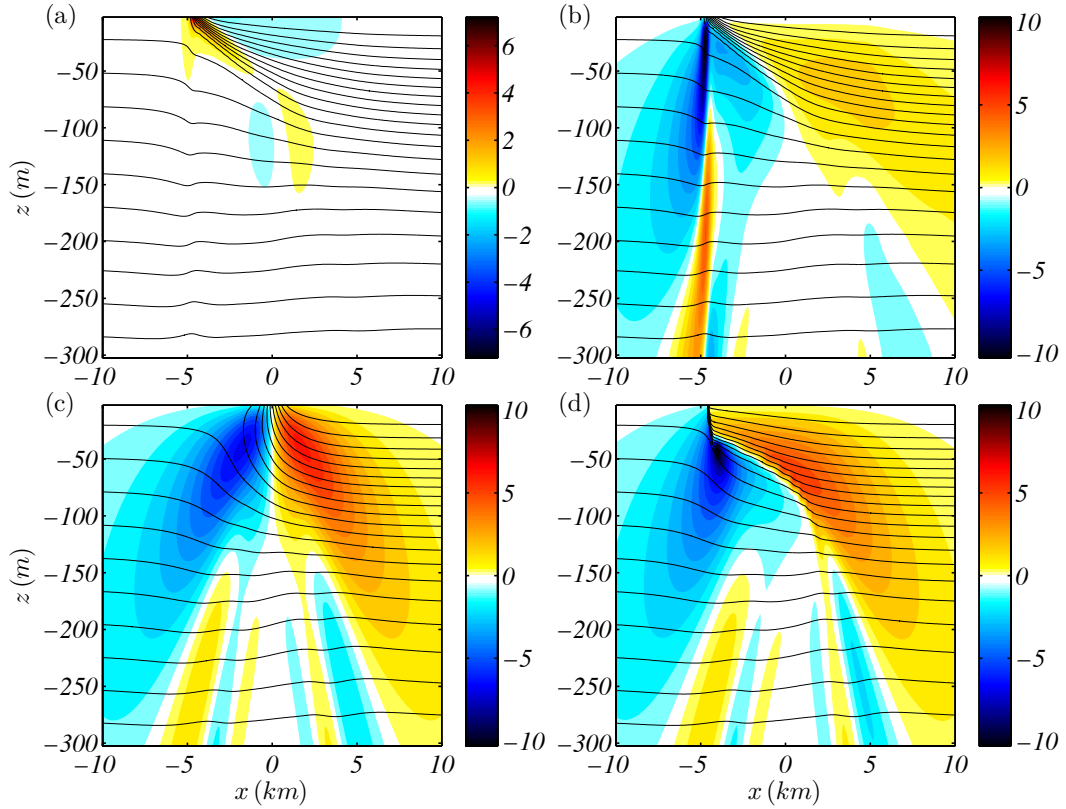
820 FIG. 5. Vertical velocity fields for a strain rate of  $\alpha = 0.4f$  and buoyancy anomaly defined by (21), for various  
 821 frontal Burger numbers  $\epsilon_F = L_R/L$ . The velocities are in units of  $\epsilon_F \Delta b_0 f / N^2$ . Contours are logarithmically  
 822 spaced from 3 to 100% of the maximum value (0.03). Grey-dashed lines indicate the predicted slope of the  
 823 frontal jets and waves. The figure can also be viewed as a sequence of snapshots in time,  $\alpha t = \ln(\epsilon_F/0.1)$ : (a)  
 824  $\alpha t = 0$ , (b)  $\alpha t = 0.69$ , (c)  $\alpha t = 1.61$ , (d)  $\alpha t = 2.30$ , and (e)  $\alpha t = 3$ . The path of a wave packet initially located  
 825 at the origin at  $t = 0$ , with initial wavenumbers  $k_0 = 0.2/L_R$  and  $m_0 = 0.5/H$ , is shown by a solid black line on  
 826 each plot. The terminus of the line is the position of the wave packet at the time the snapshot is taken. Note that  
 827 the velocities have been non-dimensionalised by  $\epsilon_F \Delta b_0 f / N^2$ , such that the maximum velocity in (e) is 20 times  
 828 that in (a) owing to the change in  $\epsilon_F$ .



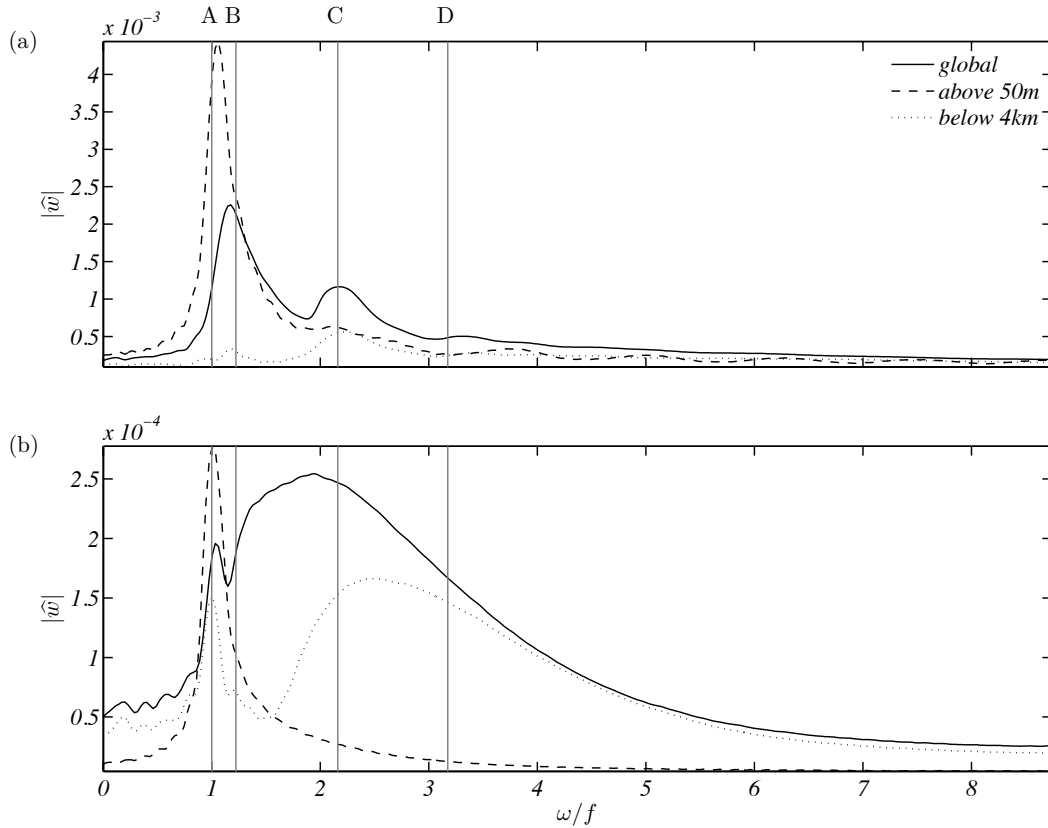
829 FIG. 6. The time evolution of the strain rate,  $\alpha(t)/f$ , and the surface buoyancy field,  $b(x,0,t)$ , in the numerical  
 830 model. A steady state is reached after about 45 hours.



831 FIG. 7. Comparison of the numerical and analytical solutions. (a) The steady state numerical vertical velocity  
 832 ( $\text{m day}^{-1}$ ) field. (b) The analytical vertical velocity field ( $\text{m day}^{-1}$ ) for the same frontal structure (see text for  
 833 details). The grey lines on each plot are the wave and jet slopes predicted from the Green's function. The region  
 834 for which  $|u| > 0.1|\bar{U}|$ , where the analytical model is expected to break down, is enclosed by a solid black line  
 835 on each plot.



836 FIG. 8. Comparison of the numerical and analytical solutions near the surface front. (a) The vorticity Rossby  
 837 number  $Ro = f^{-1} \partial_x v$  in the numerical model steady state. (b) The vertical velocity field (m day<sup>-1</sup>) and buoyancy  
 838 contours in the numerical model steady state. (c) The vertical velocity field (m day<sup>-1</sup>) and buoyancy contours  
 839 predicted by the analytical model. (d) The vertical velocity field (m day<sup>-1</sup>) and buoyancy contours of the ad-hoc  
 840 non-linear analytical model (see text for detailed description).



841 FIG. 9. Spatially averaged vertical velocity frequency spectra  $\langle |\hat{w}| \rangle$  (m) from the numerical solution when  
 842 the strain is turned off (a) instantaneously (33) and (b) gradually (34). Three lines are displayed on each plot  
 843 for the global average spectrum (solid), near-surface spectrum (above 50m, dash) and deep spectrum (below  
 844 4km, dotted). The vertical grey lines labelled A to D indicate the specific frequencies of interest: A = inertial  
 845 frequency, B = secondary circulation ‘frequency’, C = first wave mode frequency, and D = second wave mode  
 846 frequency, as predicted from the constant strain analytic model for a strain rate of  $\alpha = 0.4f$ .